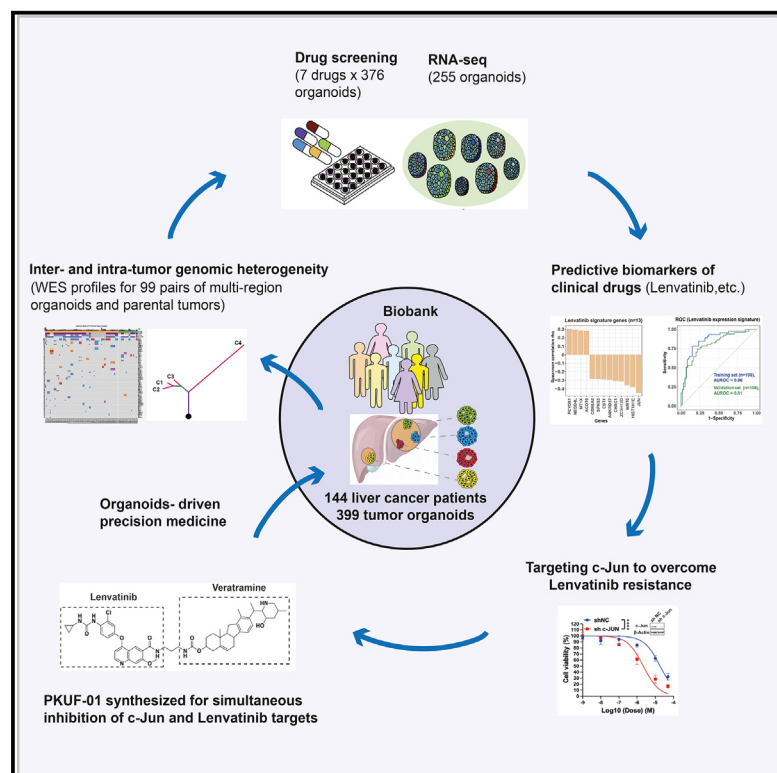


# Pharmacogenomic profiling of intra-tumor heterogeneity using a large organoid biobank of liver cancer

## Graphical abstract



## Authors

Hui Yang, Jinghui Cheng,  
Hao Zhuang, ..., Jianguo Zhang,  
Jianmin Wu, Ning Zhang

## Correspondence

zhangjg@zzu.edu.cn (J.Z.),  
wujm@bjmu.edu.cn (J.W.),  
zhangning@bjmu.edu.cn (N.Z.)

## In brief

Yang et al. reveal the genomic and phenotypic inter- and intra-tumor heterogeneity of liver cancer using a biobank of 399 tumor organoids from 144 patients. Pharmacogenomic profiling and mechanistic investigation generate biomarker panels predicting drug responses and identify c-Jun overexpression as a key factor leading to lenvatinib resistance.

## Highlights

- Analyses of multi-region organoids reveal inter- and intra-tumor heterogeneity in PLC
- Expression biomarkers are developed for predicting responses to four clinical drugs
- c-Jun is identified as a mediator of lenvatinib resistance via JNK and  $\beta$ -catenin
- c-Jun inhibition and lenvatinib exhibit a marked synergistic effect



## Article

# Pharmacogenomic profiling of intra-tumor heterogeneity using a large organoid biobank of liver cancer

Hui Yang,<sup>1,11</sup> Jinghui Cheng,<sup>1,11</sup> Hao Zhuang,<sup>2,11</sup> Hongchuan Xu,<sup>3,11</sup> Yinu Wang,<sup>1,11</sup> Tingting Zhang,<sup>2</sup> Yinmo Yang,<sup>4</sup> Honggang Qian,<sup>5</sup> Yinying Lu,<sup>6</sup> Feng Han,<sup>2</sup> Lihua Cao,<sup>7,8</sup> Nanmu Yang,<sup>2</sup> Rong Liu,<sup>1</sup> Xing Yang,<sup>3</sup> Jianguo Zhang,<sup>9,\*</sup> Jianmin Wu,<sup>7,8,\*</sup> and Ning Zhang<sup>1,8,10,12,\*</sup>

<sup>1</sup>Translational Cancer Research Center, Peking University First Hospital, Beijing, China

<sup>2</sup>Department of Hepatobiliarypancreatic Surgery, Affiliated Cancer Hospital of Zhengzhou University and Henan Cancer Hospital, Zhengzhou, China

<sup>3</sup>Department of Nuclear Medicine, Peking University First Hospital, Beijing, China

<sup>4</sup>Department of Hepatobiliary and Pancreatic Surgery, Peking University First Hospital, Beijing, China

<sup>5</sup>Key Laboratory of Carcinogenesis and Translational Research (Ministry of Education/Beijing), Department of Hepato-Pancreato-Biliary Surgery, Peking University Cancer Hospital & Institute, Beijing, China

<sup>6</sup>Comprehensive Liver Cancer Department, The Fifth Medical Center, Chinese PLA General Hospital, Beijing, China

<sup>7</sup>Key Laboratory of Carcinogenesis and Translational Research (Ministry of Education/Beijing), Center for Cancer Bioinformatics, Peking University Cancer Hospital & Institute, Beijing, China

<sup>8</sup>International Cancer Institute, Peking University Health Science Center, Beijing, China

<sup>9</sup>Department of Cancer Epidemiology, Affiliated Cancer Hospital of Zhengzhou University and Henan Cancer Hospital, Zhengzhou, China

<sup>10</sup>Yunnan Baiyao Group, Kunming, China

<sup>11</sup>These authors contributed equally

<sup>12</sup>Lead contact

\*Correspondence: zhangjg@zzu.edu.cn (J.Z.), wujm@bjmu.edu.cn (J.W.), zhangning@bjmu.edu.cn (N.Z.)

<https://doi.org/10.1016/j.ccell.2024.03.004>

## SUMMARY

Inter- and intra-tumor heterogeneity is a major hurdle in primary liver cancer (PLC) precision therapy. Here, we establish a PLC biobank, consisting of 399 tumor organoids derived from 144 patients, which recapitulates histopathology and genomic landscape of parental tumors, and is reliable for drug sensitivity screening, as evidenced by both *in vivo* models and patient response. Integrative analysis dissects PLC heterogeneity, regarding genomic/transcriptomic characteristics and sensitivity to seven clinically relevant drugs, as well as clinical associations. Pharmacogenomic analysis identifies and validates multi-gene expression signatures predicting drug response for better patient stratification. Furthermore, we reveal c-Jun as a major mediator of lenvatinib resistance through JNK and  $\beta$ -catenin signaling. A compound (PKUF-01) comprising moieties of lenvatinib and veratramine (c-Jun inhibitor) is synthesized and screened, exhibiting a marked synergistic effect. Together, our study characterizes the landscape of PLC heterogeneity, develops predictive biomarker panels, and identifies a lenvatinib-resistant mechanism for combination therapy.

## INTRODUCTION

Primary liver cancer (PLC) is the third leading cause of cancer-related deaths worldwide,<sup>1</sup> which comprises hepatocellular carcinoma (HCC), intra-hepatic cholangiocarcinoma (ICC), and a type of combined hepatocellular-cholangiocarcinoma (CHC).<sup>2–4</sup> Patients are often diagnosed with PLC at advanced stages when systemic therapies are needed,<sup>5</sup> including sorafenib or lenvatinib in the first line,<sup>6</sup> and regorafenib<sup>7</sup> or apatinib<sup>8</sup> in the second line. However, these multi-kinase inhibitors only provide minor improvement of overall survival and a marginal increase in quality of life, representing an urgent challenge for patient selection.<sup>9</sup>

Inter- and intra-tumor heterogeneity (ITH) has been indicated as a major obstacle to effective cancer treatment.<sup>10</sup> Previous studies revealed a substantial level of genomic heterogeneity in HCC,<sup>11,12</sup> ICC,<sup>13,14</sup> and CHC,<sup>15</sup> reflecting a diverse collection of cells harboring distinct molecular signatures, with implications in determining drug sensitivity and contribution to treatment failure.<sup>16–18</sup>

Patient-derived organoid (PDO) culturing has been demonstrated as a powerful instrument to recapitulate tumor heterogeneity and investigate drug sensitivity in different cancer types,<sup>19–22</sup> including for disease modeling and drug screening in PLC.<sup>23–28</sup> Nevertheless, previous efforts with PLC organoids were limited by the number of included samples and a paucity



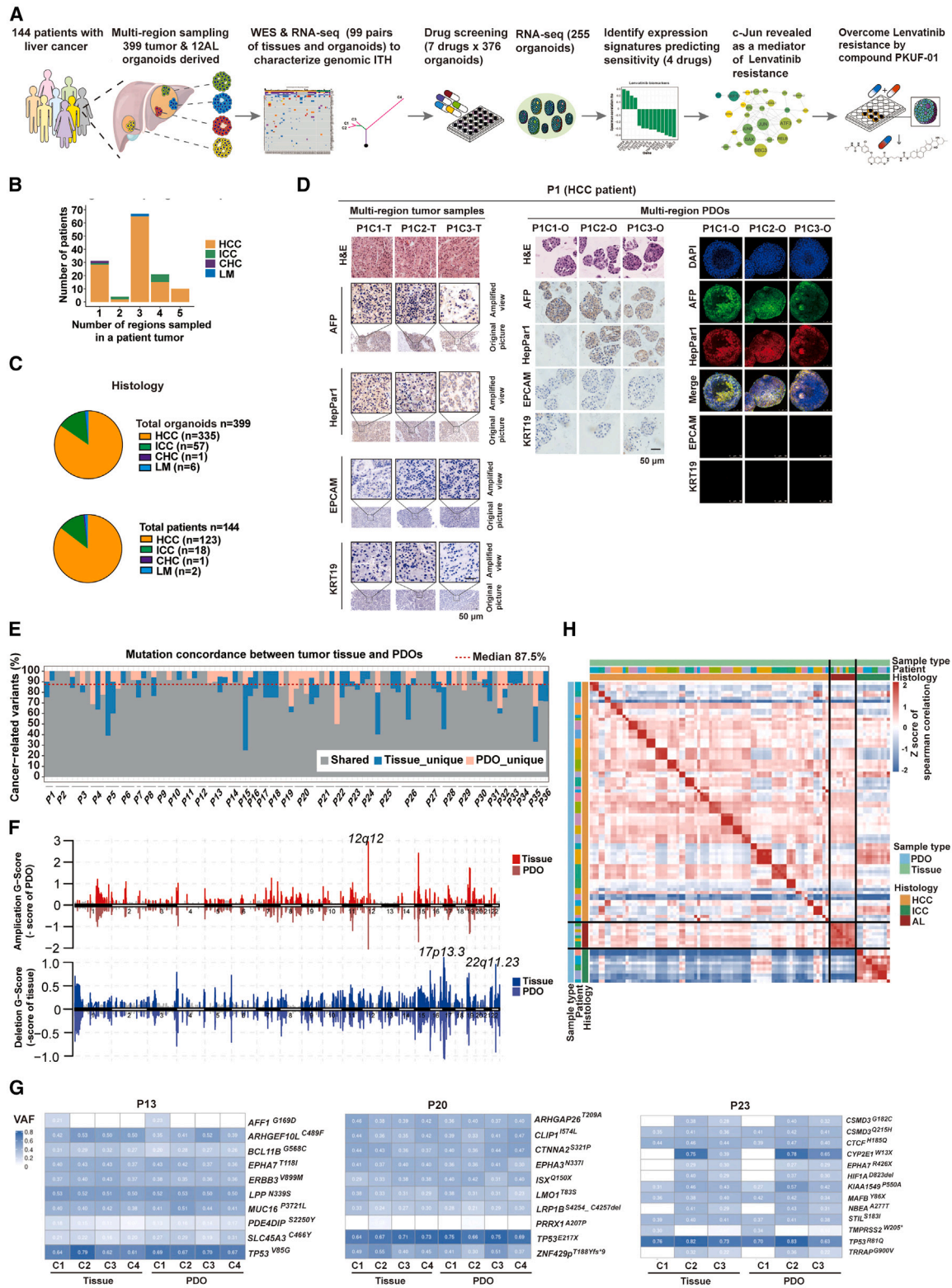


**Figure 1. A biobank of multi-region organoids recapitulated histological, genomic, and transcriptomic features of liver cancer**  
(A) A schematic summary of the study. Multi-region samples were obtained from tumors undergoing surgery resection (clinical information detailed in Table S1) and processed for organoid culturing and genomic analyses subsequently. By applying WES, RNA-seq, and drug screening, we characterized the landscape of PLC heterogeneity, developed predictive biomarkers, and revealed a lenvatinib-resistant mechanism for combinatory therapy by a compound comprising moieties of lenvatinib and veratramine (c-Jun inhibitor).

(legend continued on next page)

of multi-region samples to interrogate genomic and functional ITH simultaneously. Therefore, development of a large-scale living biobank of PLC organoids with multiple-region sampling would allow an extensive characterization of tumor heterogeneity, development of predictive biomarkers for patient stratification, and revealing mechanisms underlying drug resistance for identifying novel treatment opportunities.

Here, we established a living biobank of 399 tumor organoids, derived from spatially distinct regions of surgical specimens from 144 patients with liver cancer. Utilizing this living biobank, we dissected genomic and phenotypic heterogeneity, screened clinically relevant agents with patient response compared, identified predictive molecular biomarkers, and revealed lenvatinib resistance mechanism guiding the development of a compound (linking lenvatinib and a c-Jun inhibitor) with a marked synergistic effect.

## RESULTS

### A biobank of multi-regional organoids recapitulated histological, genomic, and transcriptomic features of liver cancer

We established a living biobank of liver cancer PDOs utilizing a multi-regional sampling strategy that represented spatially distinct regions from the resected specimens of 144 patients with liver cancer (Figure 1A). Briefly, we collected 1–5 regions from each tissue sample (Figure 1B), including 522 regions from primary tumors, six regions from liver metastases, and 30 regions from adjacent liver (AL) tissue. In total, 399 tumor organoids (75.6% overall establishment rate) and 12 normal organoids were successfully established, from 142 patients with primary tumors (123 HCC, 18 ICC, and 1 CHC patients) and two patients with liver metastases (Table S1). Sample acquisition time, the proportion of viable cells, and methods of digestion were identified as important factors impacting establishment rate (See STAR methods). Further, tumor organoids ( $n = 376$ , Data S1.1) derived by multiple-region sampling were screened with seven agents approved for therapeutic intervention in liver cancer. Based on H&E staining, we observed the similar histopathology between organoids and parental tissue (Figure 1C), and the derived organoids presented a diversity of morphologies, ranging from solid/compact structures (HCC and CHC) to more irregularly shaped cyst-like structures (ICC) (Data S1.2). Pathological marker analysis demonstrated that multi-regional organoids precisely display HCC markers (HepPar1/AFP) and ICC markers

(KRT19/EPCAM) as parental tumor tissue for both HCC (Figures 1D and Data S1.3A) and ICC (Data S1.3B) patients, while CHC organoids showed positive signals for both HCC marker (AFP) and ICC marker (EPCAM) (Data S1.3C). Subcutaneous xenografts by PDOs implanted in immunodeficient mice also recapitulated parental tumor histopathology (Data S1.4). Additionally, organoids derived from AL tissue appeared different from PLC organoids with a decreased nucleoplasmic ratio (Data S1.5), and some AL organoids grew as a single-layered epithelium of ductal-like cells surrounding a central lumen, as observed previously.<sup>23</sup>

To assess whether the developed organoid biobank recapitulated the inter- and intra-tumor heterogeneity of PLC tissue, we performed whole-exome sequencing and RNA sequencing (RNA-seq) for 99 pairs of derived organoids (randomly selected from the first 200 established organoids) and parental tumor tissue (88 HCC and 11 ICC) from 36 patients (32 patients with multi-regions sampled). Additional 156 PDOs were profiled by RNA-seq to have a total of 255 PDOs with both transcriptome and drug screening profiles (Figure 1A), for developing predictive biomarkers. First, we found a comparable mutation load between tumor tissue (median 2.43 Mutation/MB) and organoids (2.37 Mutation/MB). Consistent with previous genomic study using PLC tissue,<sup>15</sup> recurrently mutated genes, including *TP53* (43%), *AXIN1* (11%), and *CTNNB1* (9%), were identified in the organoid biobank (Figure S1A). Second, a median concordance of 87.5% cancer-related mutations (See STAR methods) was found between tumor tissue and organoids (Figure 1E). Although most samples showed a high or even full concordance, we noticed less concordance in few samples (from P5, P15, P25, and P26), implying potential tumor evolution during passaging of these organoids, as evidenced in a previous study.<sup>19</sup> Thus, we made a further comparison between early and late passages of 15 organoid lines, and found that the majority of mutations retained in both passages (the median concordance with tumor tissue: 80% for early passage and 75% for late passage), although a small subset of mutations was either lost or gained during serial passaging (Figures S1B and S1C). Third, both mutational spectrums (Figure S1D) and significant copy number alteration (CNA) peaks (e.g., 12q12, 17p13.3, and 22q11.23, Figure 1F) were highly similar between parental tumor and derived organoids. Last, most clonal and subclonal mutations of liver cancer-related genes were reserved in the PDOs (Figure 1G), such as clonal *TP53* mutations in P13, P20, and P23, and subclonal *HIF1A* mutations in P23, indicating clonal architecture could be retained in organoids.<sup>20</sup>

(B) Histogram summarizing the number of regions sampled from 144 patients, with colors indicating the histological subtypes of 142 patients with PLC and two patients with liver metastasis (LM), respectively.

(C) Pie charts illustrating the histological subtypes of all 399 organoids shown in Data S1.2 and Data S1.7, with numbers indicated in the brackets.

(D) H&E and IHC staining of three tumor regions from an HCC patient P1, and H&E, IHC, and immunofluorescence staining of the corresponding organoids. HCC markers (AFP and HepPar1) and biliary markers (EPCAM and KRT19) were assayed by IHC and immunofluorescence staining. Scale bars indicate 50  $\mu$ m.

(E) Concordance of cancer-related somatic genomic variants between tumor tissue and organoids. Median concordance is indicated. (F) Genome-wide comparison of copy number alterations (CNAs) between tumor tissue and organoids. Copy number gain (upper panel) and loss (bottom panel) peaks were plotted separately.

(G) Heatmap comparing mutation VAFs of COSMIC cancer genes between tumor tissue and PDOs for three representative HCC patients. VAF, variant allele frequency.

(H) Heatmap showing correlation between tumor tissue and paired organoids transcriptome. Samples from a same patient were grouped together, and patients were organized by histology subtype. Rows represent organoids and columns represent tissues. AL, adjacent liver. See also Figure S1, Data S1 and Tables S1-S4.

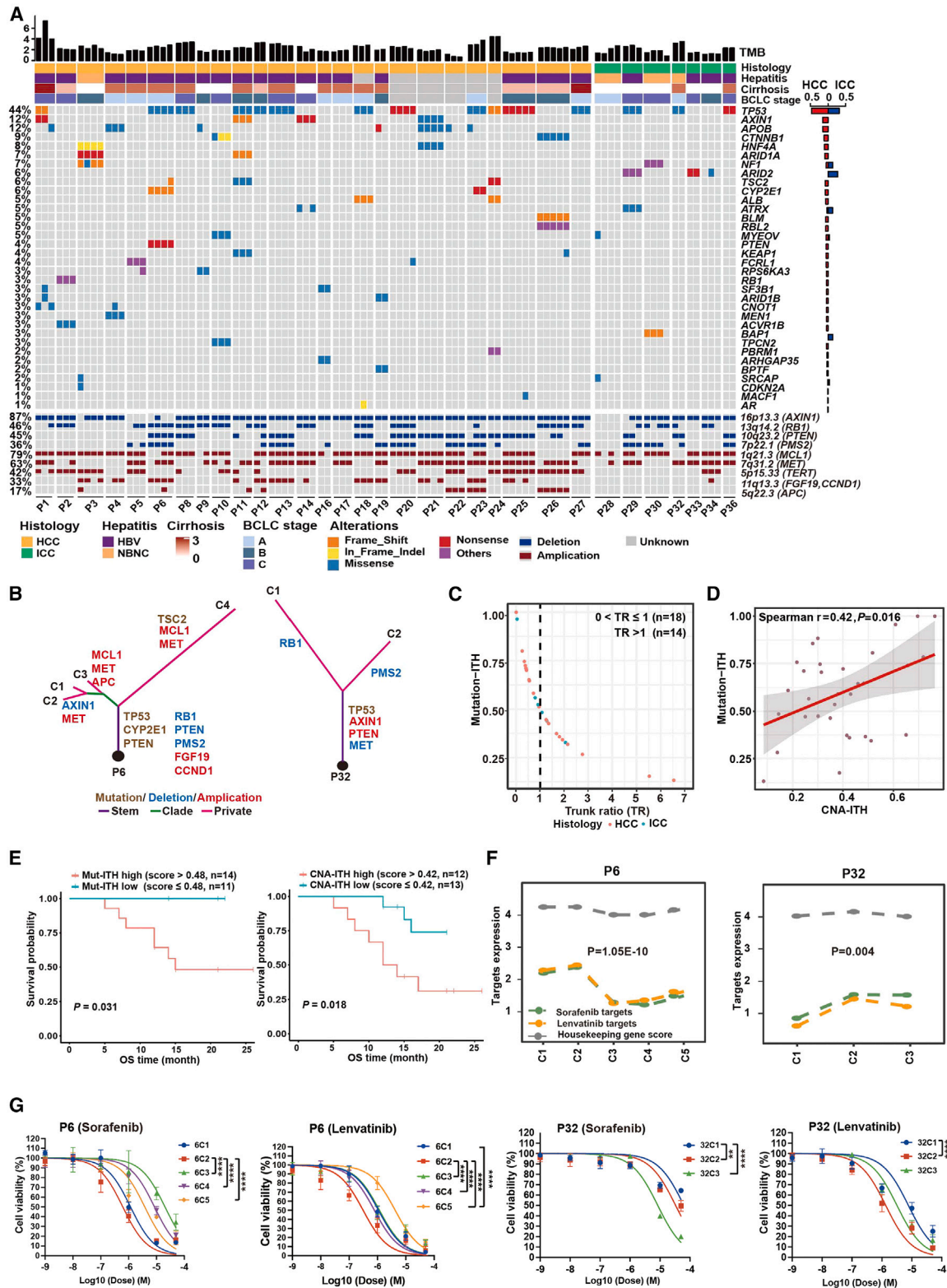


**Figure 2. Analysis of multi-regional organoids characterized the genomic ITH and associated functional implications**

(A) Genomic landscape of 95 PLC organoids derived from 32 patients with multi-region sampling. Top panel shows the burden of somatic non-silent mutations, histology, hepatitis status, cirrhosis, and stage information. Middle panel details somatic simple mutations in liver cancer-related genes with rightmost bars representing mutation frequency in HCC and ICC. Bottom panel shows genes with CNAs.

(legend continued on next page)

Further expression analysis identified a high level of correlations between paired tumor and organoids at transcriptome level ( $n = 99$  pairs) (Figure 1H) using a published strategy,<sup>23</sup> and similar expression correlations with tumor tissue were also shown in both early and late organoid cultures (Figure S1E). By analyzing RNA-seq profiles of the panel of PLC marker genes,<sup>23</sup> a high expression of HCC markers (*AFF*, *GPC3*) and hepatocyte markers (*ALB*, *TTR*, *APOA1*, *APOE*) was found in HCC organoids and parental tumor tissue (Figure S1F), whereas cholangiocarcinoma markers (*KRT19*, *EPCAM*, *S100A11*) were highly expressed in ICC organoids and tissues. Furthermore, subtyping results of HCC PDOs using a published HCC transcriptomic classification<sup>29</sup> showed a significant consistence (93.75%) with the subtyping results using HCC tissue ( $p = 6.1e-21$ ) (Figure S1G).

Together, our comprehensive comparative analyses demonstrated that the derived PLC PDOs retained the histopathological characteristics and genomic and transcriptomic features of parental tissues, which would be versatile for investigating PLC inter- and intra-tumor heterogeneity.

#### Analysis of multi-regional organoids characterized genomic ITH of liver cancer with functional implications

We investigated genomic ITH of 32 PLC patients with established and sequenced multi-regional PDOs (Figure 2A), with a substantial level of genomic ITH identified. First, a sub-group of patients, including P1, P4, P6, and P23, showed clear variation in tumor mutation burden (TMB) among multiple-region samples. Next, multiple PLC cancer-related genes were found to have heterogeneous somatic mutations and/or CNAs across regions sampled from a same tumor. For example, two regions of P1 (P1C1 and P1C2) harbored oncogenic *TP53* and *AXIN1* mutations, whereas undetected in the third region (P1C3). Meanwhile, P1C3 had a unique oncogenic *APOB* mutation and an additional *RB1* deletion (Figure 2A). Additionally, *APOB* mutation was identified in only single region for another four patients including P9, P19, P22, and P23. Deletion of chromosomal regions containing tumor suppressor genes, including 16p13.3 (*AXIN1*), 12q14.2 (*RB1*), and 10q23.2 (*PTEN*), was also found to be heterogeneous in a subset of patients.

To systematically characterize genomic ITH, we constructed phylogenetic trees for individual patient, by applying maximum-parsimony algorithm based on identified somatic point mutations (Figures 2B and S2A). A number of frequent trunk events in PLC were identified, including mutations in *TP53*, *RB1*, *AXIN1*, and *CCND1*, which were consistent with a previous study.<sup>30</sup> Based on the trunk ratio, i.e., the ratio of ubiquitous mutations to non-

ubiquitous mutations, phylogenetic trees of 12 patients were regarded as trunk dominant (trunk ratio  $> 1$ ), while the other 20 patients as branch dominant (Figure S2A). Decreased trunk ratio appeared to be associated with higher ITH (Figure 2C). Moreover, there was a positive correlation shown between mutation-ITH and CNA-ITH (Figures 2D and S2B), and both mutation-ITH and CNA-ITH levels showed significant associations with patient outcome in our cohort (Figure 2E). PLC patients with a higher level of mutation/CNA-ITH had worse overall survival (both  $p < 0.05$ ). In addition, tumors with hepatitis B virus infection (based on pathological assessment) presented significantly lower levels of ITH (Figure S2C).

Next, we speculated that genomic and associated transcriptomic heterogeneities might result in heterogeneity in drug sensitivities. Expression of target genes for PLC first-line agents sorafenib and lenvatinib was investigated with 255 PDOs from 79 patients. Notably, some patients, e.g., P6 and P32, showed substantially variable expression of target genes in organoids derived from diverse regions (Figures 2F and S2D), indicating a possible intra-tumor heterogeneity in drug response. For confirmation, we treated multiple organoid cultures from patients P6 and P32 with these two agents and found that the regions with a reduced level of target gene expressions showed an increased drug resistance (Figures 2F and 2G).

Overall, we revealed an extensive level of genomic ITH in PLC, which showed a prognostic association and might lead to heterogeneous response to drug treatment.

#### Screening of clinically relevant agents predicted patient response and revealed intra-tumor heterogeneity in drug sensitivity

We performed screening of 7 PLC-relevant agents in 376 organoids derived from 116 patients (Figure 3A), which included the first-line agents lenvatinib and sorafenib,<sup>6</sup> the second-line agents regorafenib<sup>7</sup> and apatinib,<sup>8</sup> anti-VEGFR antibody bevacizumab,<sup>31</sup> as well as agents targeting ICC with actionable mutations, including pemigatinib (targeting cholangiocarcinoma harboring FGFR2 fusions/rearrangements)<sup>32</sup> and ivosidenib (targeting IDH1-mutant, chemotherapy-refractory cholangiocarcinoma).<sup>33</sup>

Two common summary statistics, half-maximal inhibitory concentration (IC50) (Figure 3B) and normalized area under the curve (AUC) (Figure 3C) were calculated, and a strong correlation was observed between the IC50 and AUC values for each of the 7 screened drugs (Spearman  $r > 0.79$ ) (Figure 3D). We regarded the maximum IC50 (or AUC) value among all regions from a patient as the patient-level IC50 (or AUC) value, based on the assumption that a patient's response to a drug treatment was

(B) Phylogenetic trees of two representative patients with potential driver events indicated. See Figure S2 for the phylogenetic trees of additional patients.

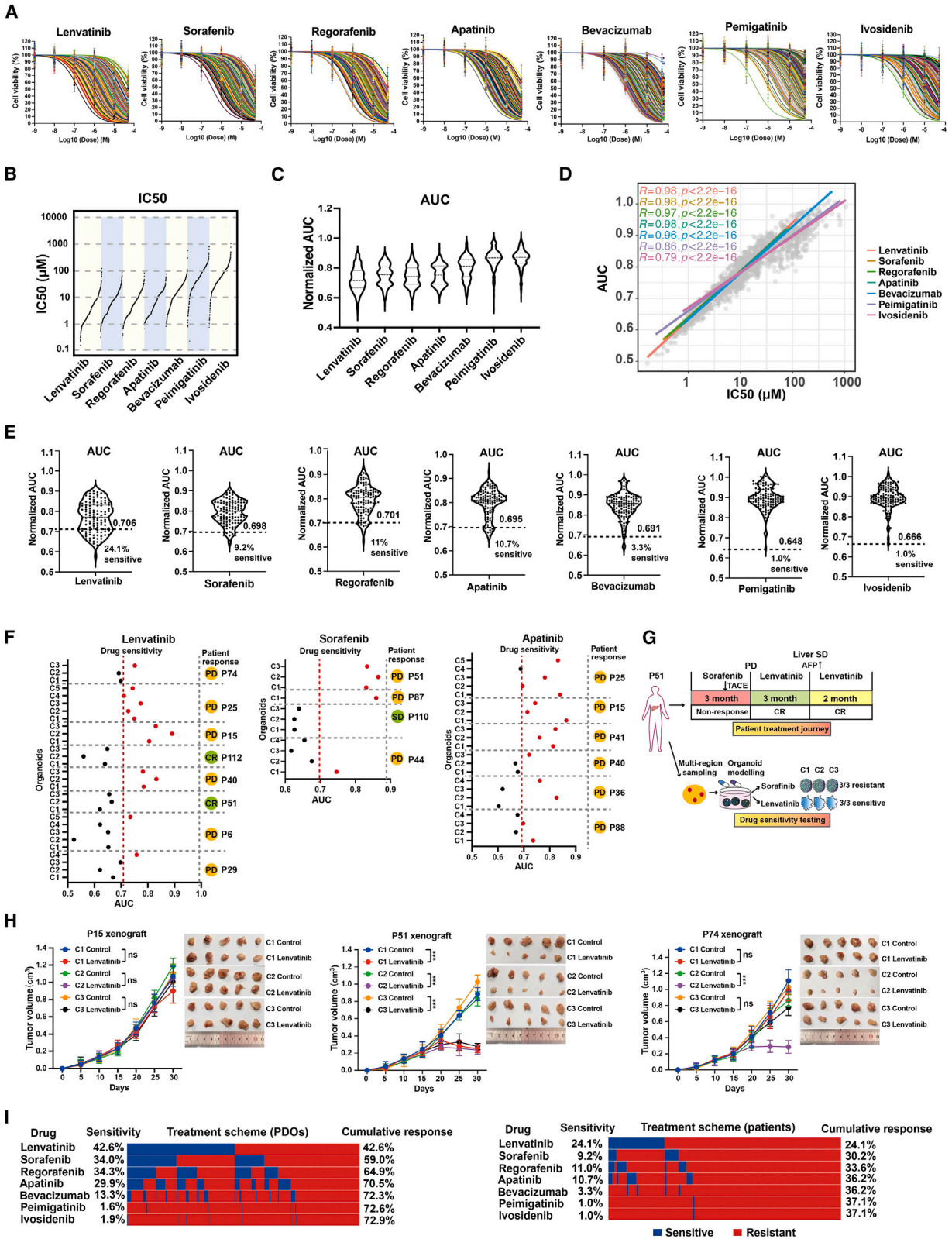
(C) Scatterplot depicting the trunk ratio (TR) of mutations for each of 32 patients, in which 12 patients are trunk dominant ( $TR > 1$ ) and 20 patients are branch dominant ( $TR \leq 1$ ).

(D) Scatterplot showing positive correlation between mutation-ITH and CNA-ITH levels.

(E) Kaplan-Meier survival curves illustrating the association of mutation-ITH (left) and CNA-ITH (right) with overall survival, respectively.  $p$  value determined by two-sided log rank test.

(F) Average expression of known sorafenib and lenvatinib targets in organoid cultures derived from patients P6 (5 organoids) and P32 (3 organoids). Dotted line connects multiple organoids from the same tumor.  $\log_2$  (TPM+1) was referred as drug target expression, while expression level of housekeeping genes was used as the control (See STAR methods). ANOVA was used to test the statistical significance for difference of target expression between multiple regions of a tumor.

(G) Dose-response curves of sorafenib and lenvatinib for organoid cultures from patients P6 and P32. Data represent relative cell viability values, with DMSO-treated organoids as control. Error bars represent means  $\pm$  SD from at least triplicate experiments. \*\* $p < 0.01$ ; \*\*\*\* $p < 0.0001$ . See also Figure S2, Tables S2 and S5.



(legend on next page)

determined by the most resistant region. All patients were ranked by patient-level AUC and dichotomized into sensitive and resistant groups for each drug, respectively, using the percentile cutoff according to the reported clinical overall response rate (See STAR methods, Figure 3E). By testing drug sensitivity in the early and late organoids passages of 16 organoids, we found that most organoids (12/16) showed nearly identical sensitivity to lenvatinib treatment between the early and late passages, while differences were observed in four organoids P61C3, P75C2, P76C2, and P133 (Figure S3A). Based on the AUC cutoffs, these four PDOs were non-sensitive to lenvatinib at early passage and became even more resistant at late passage. We speculated that these four organoids consisted of non-homogenous population with expansion of resistant population during passaging.

Next, we compared the organoids-based drug sensitivity results with the corresponding clinical response, based on investigations of 14 patients who were relapsed during the study period and had treatment with at least one of studied drugs, including lenvatinib (n = 8), sorafenib (n = 4), and apatinib (n = 6) (Figure 3F). In eight patients with lenvatinib treatment, two patients (P51 and P112) underwent complete response (CR), with organoids derived from all three regions showing sensitivity, while the other six patients underwent progressive disease, with organoid(s) derived from at least one region being resistant to lenvatinib. Therefore, clinic response appeared to support the lenvatinib sensitivity results using organoids (p = 0.036) (Figure 3F). Similar comparisons with sorafenib and apatinib also confirmed the prediction value of our organoid drug screening (Figure 3F).

Furthermore, 4 out of 14 patients experienced therapeutic regimen change after assessing the response based on mRECIST criteria during the study period. For example, patient P51 was non-responsive to sorafenib and transcatheter arterial chemoembolization treatment, but later underwent CR to lenvatinib for a total of five months (Figure 3G). In line with the clinical responses, all three organoids from P51 were found to be resistant to sorafenib but sensitive to lenvatinib. Another example was patient P15, who showed no clinical response to monotherapy treatment of lenvatinib, apatinib, and bevacizumab sequentially (Figure S3B). Accordingly, all three organoids from P15 showed resistance to

lenvatinib and apatinib, and two organoids were resistant to bevacizumab.

The results from organoid drug screening were also validated using organoid-derived xenografts (Figure 3H). Organoids from patients P15, P51, and P74 were transplanted to immune-deficient mice and treated with lenvatinib, respectively. All the xenografts derived from drug-sensitive organoids showed inhibitory effects upon lenvatinib treatment. Taken together, these results demonstrated the clinical potential of applications of PLC organoids in predicting patient treatment response.

Last, we utilized drug screening results to quantitatively assess the potential benefits of seven targeted therapy drugs used in current clinical practice for PLC patients. A striking difference between region (organoid) level and patient level was estimated for both individual and cumulative sensitivity (Figure 3I). Although a cumulative sum of 72.9% sensitivity could be achieved for all derived organoids from different regions, only 37.1% patients may benefit from the monotherapy with any of these agents considering the most insensitive organoid from a patient, which may be due to extensive ITH in PLC. Additionally, we screened 50 ICC organoids with gemcitabine and cisplatin, two chemotherapeutic agents used for patients with advanced biliary tract cancer,<sup>34</sup> and found a subgroup of ICC organoids insensitive to gemcitabine (n = 10, 32%) or cisplatin (n = 9, 29%) could benefit from lenvatinib (Figure S3C), respectively. Thus, it requires precise approaches to stratify PLC patients for targeted therapy treatment.

### Molecular analysis identified expression signatures predicting sensitivities to lenvatinib and three other drugs

As genomic heterogeneity has been recognized as a major factor contributing to drug resistance,<sup>35</sup> we first investigated the association of genomic heterogeneity with PLC drug sensitivities using our multi-regional PDOs. Significantly elevated levels of mutation ITH and CNA-ITH were both identified in the lenvatinib-resistant group of patients than the sensitive group (Figure 4A), indicating a role of ITH in resistance of lenvatinib treatment. We also investigated the associations of genomic ITH with sorafenib, regorafenib, and apatinib sensitivities (Figures S4A–S4C), respectively, and found an increased level of CNA-ITH in the apatinib-resistant group of patients. However, it is

**Figure 3. A large-scale drug screening using the living biobank and agreements with patient responses**

(A) Dose-response curves of seven targeted drugs (sorafenib, lenvatinib, regorafenib, apatinib, bevacizumab, pemigatinib, and ivosidenib) for all screened 376 organoids (from 116 patients). Data represent relative cell viability values, with DMSO-treated organoids used as control. Error bars represent means  $\pm$  SD from at least triplicate experiments.

(B) Scatterplots showing IC50 distribution of seven targeted drugs in 376 organoids.

(C) Violin plots showing normalized AUCs of seven targeted drugs in 376 organoids.

(D) Scatterplots indicating significant positive correlation between AUC and IC50 values for each of seven targeted drugs.

(E) Violin plots illustrating normalized AUCs of seven targeted drugs in 116 patients (represented by the maximum AUC value among multi-regions of a tumor). Dashed line represents the cutoff used to define the sensitive group for each drug.

(F) For relapsed patients with treatment of lenvatinib/sorafenib/apatinib, individual scatterplot shows AUC values identified by drug screening of the matched organoids, with clinical responses from patients indicated on the right for comparing the consistency. CR, complete response; PD, progressive disease; SD, stable disease.

(G) A schematic diagram illustrating patient journey (top panel) for P51 with indicated treatment after each relapse, and drug sensitivity results (bottom panel) of multi-region organoids derived from his primary tumor.

(H) Tumor growth curves of organoid-derived xenografts (left panels) originated from different tumor regions of three patients (P15, P51, and P74) with lenvatinib treatment. Tumors were imaged after the mice were sacrificed (right panels). Data are representative of five mice each group. Error bars represent means  $\pm$  SD. \*\*\*, p < 0.001; ns, not significant.

(I) A customized chart indicating the cumulative sensitivity (labeled on the right) of seven targeted drugs in the organoid biobank, at PDO level (left panel) and patient level (right panel). See also Figure S3 and Tables S6.

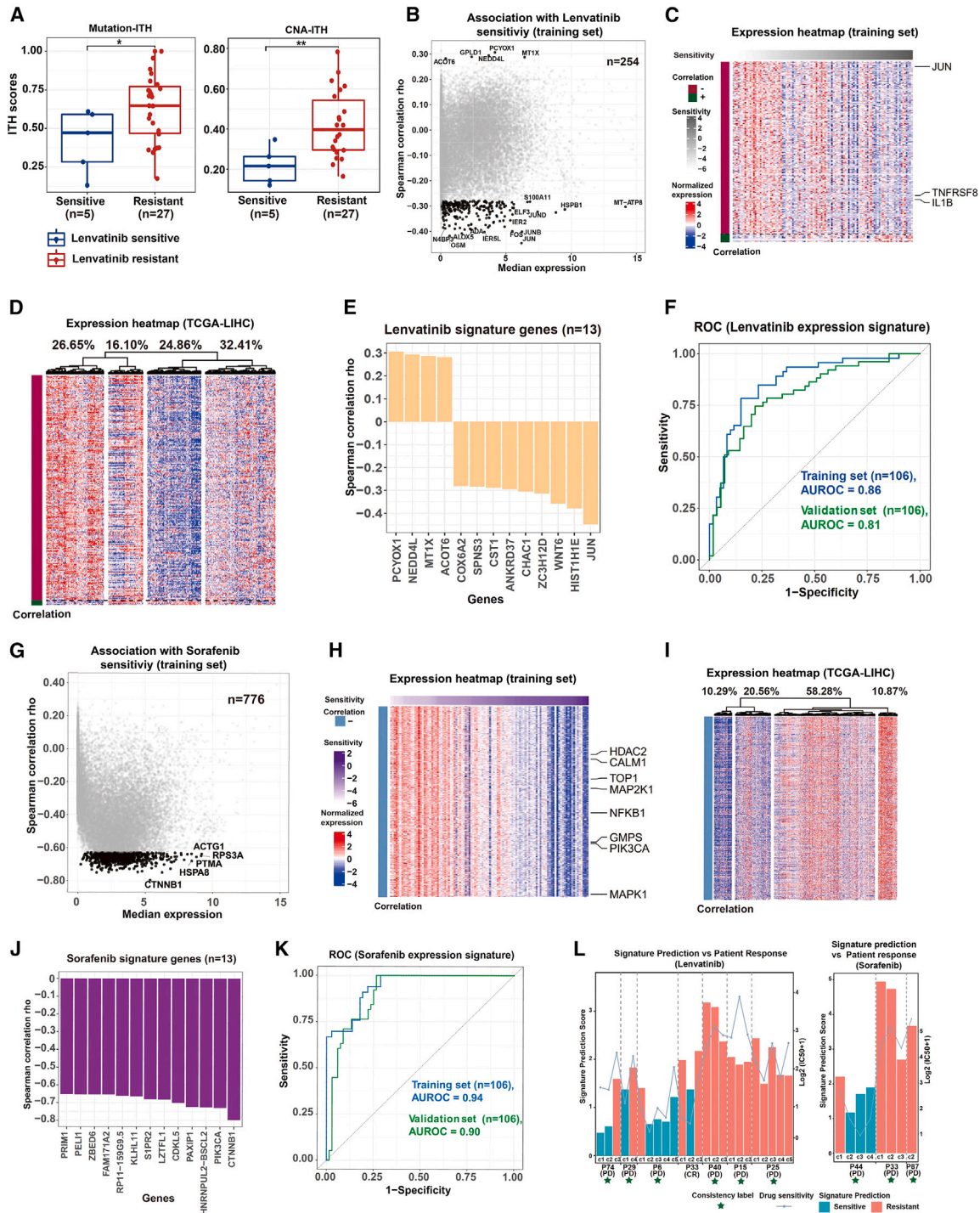


**Figure 4. Molecular analysis identified expression signatures predicting sensitivity of clinically relevant agents**

(A) Boxplots comparing the levels of genomic ITH (left: Mutation-ITH, right: CNA-ITH) between the lenvatinib-sensitive and -resistant groups of organoids. The box bounds the interquartile range divided by the median, with the whiskers extending to a maximum of 1.5 times the interquartile range beyond the box. Wilcoxon rank-sum tests, all p values are two sided, \*p < 0.05; \*\*p < 0.01.

(B) Scatterplot of protein coding genes with the horizontal axis showing median gene expression, and the vertical axis showing the expression correlations with drug sensitivity. Dots in black indicate 254 genes significantly associated with lenvatinib sensitivity.

(C) Heatmap showing the normalized expression of these 254 genes, with samples ordered by drug sensitivity, and targets of FDA-approved drugs labeled.

(D) Heatmap showing unsupervised clustering of TCGA-LIHC samples based on expression of these 254 genes.

(E) Bar plot showing expression correlations with drug sensitivity for 13 signature genes (See STAR methods) predicting lenvatinib response.

(legend continued on next page)

challenging to use genomic ITH levels as predictive biomarkers, due to a lack of specificity for individual agent.

Thus, we continued to model PLC drug sensitivities using transcriptomic profiles, as gene expression profiles have been successfully associated with patient response to drug treatment.<sup>36,37</sup> Two sets of organoids developed prospectively with both RNA-seq and drug screening profiles were used for training (n = 106) and validation (n = 106), respectively. Using the training set, we first identified 254 genes with significant associations with lenvatinib sensitivity (See STAR methods) (Figure 4B), in which three genes (*JUN*, *IL1B*, and *TNFRSF8*) are the targets of Food and Drug Administration (FDA)-approved drugs,<sup>38</sup> as indicated in the expression heatmap (Figure 4C). Using these 254 genes, we clustered 424 HCC patients from the TCGA-LIHC project<sup>39</sup> and four groups of patients were stratified. Notably, a group of patients showed ubiquitously low expression of resistant genes (Figure 4D), with a proportion (24.86%) similar to the reported clinical efficacy (24.1%) of lenvatinib,<sup>6</sup> indicating this group could be enriched of patient sensitive to lenvatinib treatment.

To identify key genes associated with drug response for biomarker development, we further applied a machine-learning-based approach (See STAR methods) and identified a panel of 13 signature genes as the predictive biomarker of lenvatinib response, including *JUN*, *HIST1H1E*, and *WNT6A* (Figures S4D and 4E). This multi-gene biomarker achieved 0.86 for area under receiver operating characteristic (AUROC) curve (Figure 4F), and showed a similar decent performance in the validation set of organoids (AUROC 0.81). Moreover, we applied the same analysis procedure to the other three PLC drugs (sorafenib, regorafenib, and apatinib), and developed predictive biomarkers for treatment response of sorafenib (AUROC >0.9 in both training and validation sets, Figures 4G–4K and S4E), regorafenib (AUROC >0.8 in both, Figures S4F–S4K), and apatinib (AUROC >0.7 in both, Figures S4L–S4Q), respectively.

Last, we evaluated the clinical utilities of the developed biomarker using patients with both treatment of studied PLC drugs during study period and multi-regional organoid analyses, in which 6 out of 7 patients with lenvatinib treatment showed consistent results between signature prediction and clinical response (Figure 4L), while a full consistency observed for patients with sorafenib treatment (3/3, Figure 4L) and patients with apatinib treatment (5/5, Figure S4R).

Taken together, we developed and validated multi-gene expression signatures predicting response of four antitumor agents used in PLC clinical practice, warranting future clinical investigation including biomarker-guided trials.

### c-Jun-mediated lenvatinib resistance

Understanding the mechanisms of lenvatinib resistance in PLC could help development of novel therapeutic options for combi-

nation treatment.<sup>40,41</sup> Lenvatinib can block VEGFR and FGFR signaling, but the mechanism of lenvatinib's effect on liver cancer organoids remains unclear. By analyzing expression levels of all known lenvatinib-targeted receptors (Figure S5A), we found that FGFRs are particularly highly expressed in PLC organoids, as well as in published cancer cell lines (n = 98, from CCLE) for four cancer types with lenvatinib approved for usage in clinic. To investigate the functional consequence, we further tested the effect of FGFR knockdown on lenvatinib sensitivity in lenvatinib-sensitive organoids, which were top five high-expression ones for each FGFR member gene, respectively (Figure S5B). FGFR1 knockdown in top five FGFR1 high-expression organoids reduced the sensitivity to lenvatinib treatment in 4 out of 5 organoids (P28C4, P41C2, P16C1, and P41C1). For the remaining FGFRs, 2/5, 3/5, and 3/5 high-expression organoids showed reduced sensitivity to lenvatinib treatment upon knocking down of FGFR2, FGFR3, and FGFR4, respectively. These results suggest that FGFRs play an important role in lenvatinib-mediated therapeutic effects in PLC organoids.

To identify lenvatinib-resistant genes, we performed protein-protein interaction (PPI) network analysis (Figure 5A) using genes significantly associated with lenvatinib sensitivity. Notably, *JUN*, a hub protein of this PPI network, is one of 13 signature genes for lenvatinib response, and the target of an FDA-approved drug. Gene expression of *JUN* was positively correlated with the resistance to lenvatinib treatment as represented by IC50 value ( $R = 0.36$ ,  $p = 2.8e-09$ , Figure 5B). Protein levels of c-Jun, assessed by immunohistochemical staining, were also significantly higher in the 216 regions with lenvatinib-resistant organoids than the 160 regions with sensitive organoids ( $p < 0.001$ , Figure 5C). In addition, higher c-Jun expression was found in tumors than paired para-cancerous tissues in 100 patients ( $p < 0.001$ , Figures 5D and S5C). Together, high level of c-Jun was found to be implicated in tumorigenesis and lenvatinib resistance in PLC.

We further investigated the functional insights, using an HCC patient (P20) and an ICC patient (P94) with organoids derived from distinct regions showing divergent response to lenvatinib treatment. An elevated level of c-Jun was shown in the lenvatinib-resistant organoids (P20C1, P20C2, and P94C2), compared to the sensitive organoids (P20C3, P20C4, and P94C1) (Figures 5C and S5D). Next, we knocked down c-Jun in P20C2 and P94C2 organoids, and found that c-Jun knockdown could sensitize lenvatinib-resistant organoids (Figure 5E). In contrast, overexpression of c-Jun in P20C3 and P94C1 converted them to be resistant to lenvatinib treatment (Figure 5F).

To systematically evaluate the role of c-Jun in lenvatinib resistance across a wide spectrum of PLC patients, we further knocked down c-Jun in 216 lenvatinib-resistant organoids, in which 63 (29.2%) were converted to be sensitive (Figure 5G).

(F) ROC curves of the 13-gene lenvatinib predictive signature in the training (n = 106) and validation (n = 106) sets. Area under ROC curves (AUROCs) are indicated.

(G–K) are counterparts for (B–F) for the expression signature predicting sorafenib response, in which 776 genes were significantly associated with sorafenib sensitivity and 13 genes were identified as the sorafenib signature genes.

(L) Bar graphs showing lenvatinib signature (left panel) and sorafenib signature (right panel) predictions for relapsed patients with both RNA-seq profiled multi-region organoids and clinical response from the treatment of individual drug. Bar colors indicate the predicted response by the expression signature, and patient clinical response are indicated at horizontal axis. Signature prediction score were indicated by the left y axis, while drug sensitivity results by the right y axis. See also Figure S4 and Tables S5 and S6.

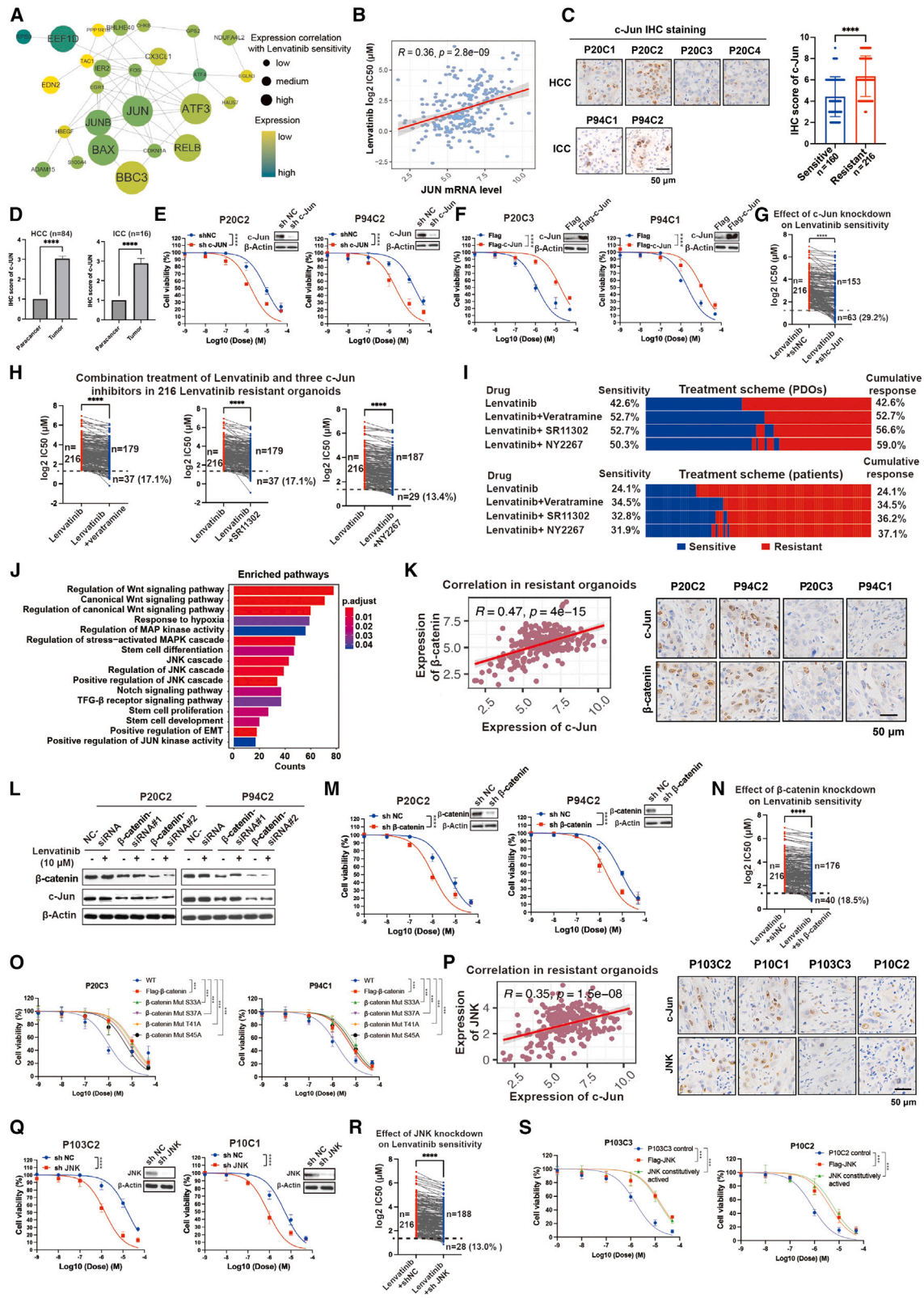


**Figure 5. c-Jun was identified as a mediator of lenvatinib resistance**

(A) An interaction network consisting of lenvatinib-resistant proteins, with the size of a circle indicating expression correlation with lenvatinib sensitivity, and the color of a circle indicating gene expression level (darker color for higher expression).

(legend continued on next page)

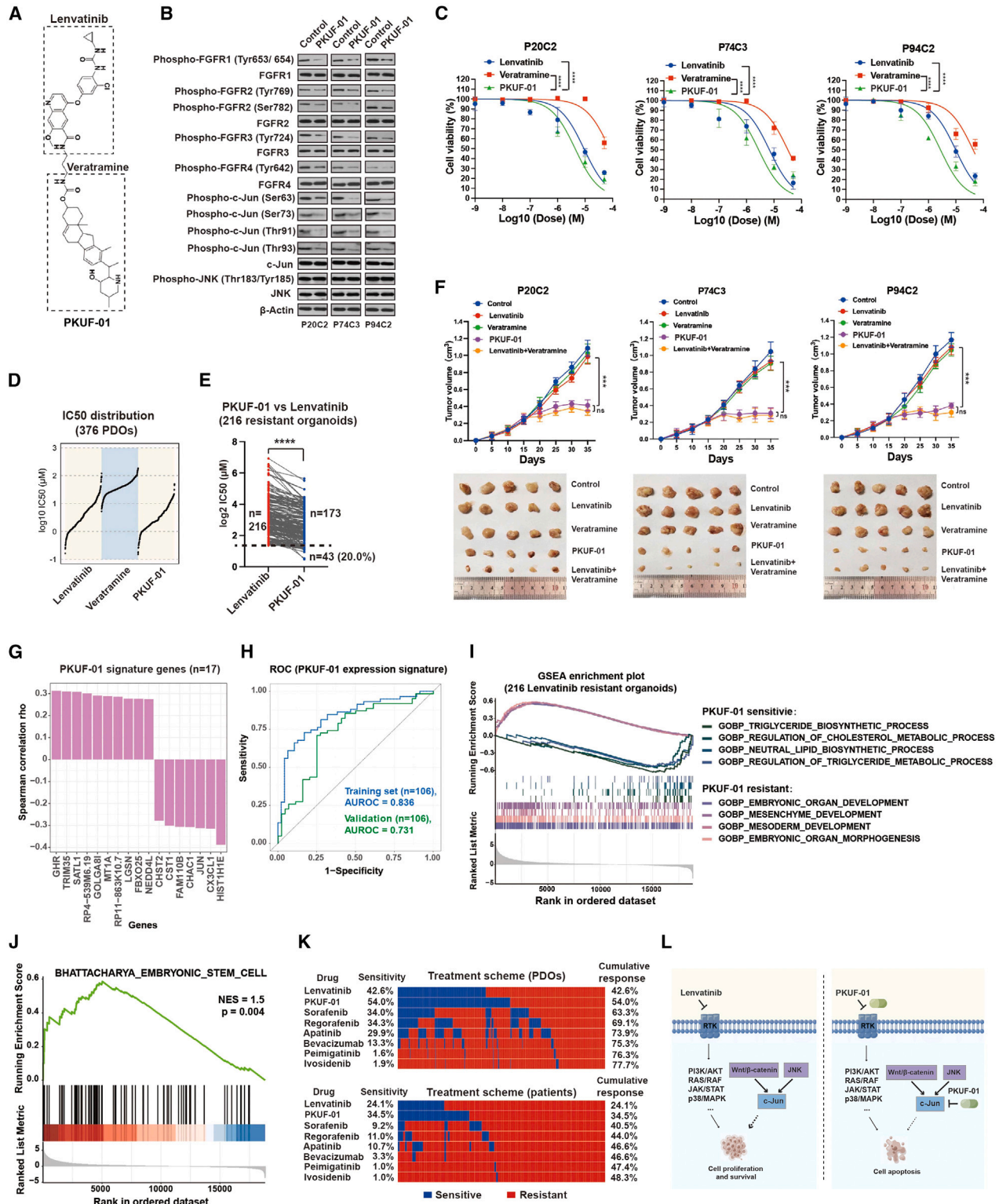
Consequently, this would potentially benefit a total of 27 patients with resistance to lenvatinib treatment (Figure S5E). Notably, 23 out of these 27 patients had a heterogeneous response to lenvatinib treatment in their organoids derived from distinct regions, implying a high level of phenotypic ITH whereas c-Jun inhibition may help address lenvatinib resistance for these patients. Therefore, we employed three c-Jun inhibitors (veratramine, SR11302, and NY2267) and found increased sensitivity to lenvatinib treatment in the previous resistant organoids, with an increase of 17.1%, 17.1%, and 13.4%, respectively (Figure 5H). Further analysis of the entire organoid biobank suggested that a maximum of 37.1% patients (59.0% of regions) could be sensitive to combinatorial treatment of lenvatinib and one of three c-Jun inhibitors (Figure 5I). Together, these results indicated that high level of c-Jun could contribute to lenvatinib resistance in PLC.

To reveal the signaling underlying c-Jun-mediated resistance to lenvatinib, we performed functional enrichment analysis using 245 genes with significant negative associations with lenvatinib response, and found that Wnt and c-Jun N-terminal kinase (JNK) signaling pathways were significantly dysregulated (Figure 5J). Expression of  $\beta$ -catenin (a key Wnt signaling regulator)<sup>42</sup> and c-Jun was found to be positively correlated (Spearman  $r = 0.47$ ) in lenvatinib-resistant organoids (Figure 5K, left). We continued functional investigation using P20 (HCC) and P94 (ICC) organoids. High levels of c-Jun and  $\beta$ -catenin were both shown in lenvatinib-resistant organoids (P20C2 and P94C2), while low levels in the sensitive organoids (P20C3 and P94C1) (Figure 5K, right). Knockdown of  $\beta$ -catenin in P20C2 and

P94C2 organoids reduced c-Jun protein levels (Figure 5L) and increased the sensitivity to lenvatinib treatment (Figure 5M). We further screened all lenvatinib-resistant organoids and found that 18.5% organoids were converted to be sensitive upon  $\beta$ -catenin knockdown (Figure 5N). In contrast, overexpression of wild-type and mutant  $\beta$ -catenin (S33A/S37A/T41A/S45A, mutation of these phospho-acceptor sites stabilizes  $\beta$ -catenin, allowing it to accumulate, translocate to the nucleus, and activate WNT signaling)<sup>43</sup> significantly reduced the sensitivity to lenvatinib treatment in both sensitive organoids (Figure 5O). These results together indicated  $\beta$ -catenin as a key regulator of c-Jun in lenvatinib-resistant organoids.

However, knockdown of  $\beta$ -catenin only partially accounts for the sensitized organoids to lenvatinib treatment upon c-Jun knockdown (18.5% versus 29.2%, Figures 5G and 5N). We continued investigation with another dysregulated signaling, JNK. A positive correlation between JNK and c-Jun expression was also found in lenvatinib-resistant regions (Spearman  $r = 0.35$ ) (Figure 5P, left panel). As P20 and P94 organoids had low expression of JNK, we selected P103 and P10 for investigation, as their multi-regional organoids presented various levels of JNK expression and showed no benefit from  $\beta$ -catenin knockdown (Figure S5F). Lenvatinib-resistant organoids P103C2 and P10C1 showed higher levels of JNK compared with the sensitive one P103C3 and P10C2 (Figure 5P, right panel), and knockdown of JNK significantly increased the sensitivity to lenvatinib treatment in both resistant organoids (Figure 5Q). Furthermore, systematic knockdown of JNK using the organoid biobank significantly improved the sensitivity to lenvatinib in 28 (13.0%) out of all 216

- (B) Scatterplot showing positive correlation between the level of lenvatinib resistance (represented by log<sub>2</sub> transformed IC<sub>50</sub> values) and mRNA expression of *JUN* among all 255 organoids with RNA-seq and drug testing profiles.
- (C) IHC staining of c-Jun (left panel) in two representative patients P20 (HCC) and P94 (ICC). IHC quantification of c-Jun with all regions of tumor tissue (right panel), showing a significant increase of c-Jun expression in the regions with lenvatinib-resistant organoids than the regions with sensitive organoids.
- (D) Histogram representing a significant increase of c-Jun protein level in HCC and ICC tissue than the paired paracancerous samples (100 pairs), assayed by immunoblotting. See Figure S5C for detailed immunoblots.
- (E) Dose-response curves of lenvatinib upon c-Jun knockdown (sh c-Jun) in two lenvatinib-resistant organoids (P20C2 and P94C2). Data are representative of at least three independent experiments. Error bars represent means  $\pm$  SD. \*\*\*\*,  $p < 0.0001$ .
- (F) Dose-response curves of lenvatinib upon c-Jun overexpression (Flag-c-Jun) in two lenvatinib-sensitive organoids (P20C3 and P94C1). Data are representative of at least three independent experiments. Error bars represent means  $\pm$  SD. \*\*\*\*,  $p < 0.0001$ .
- (G) Scatterplot showing IC<sub>50</sub> change of lenvatinib upon c-Jun knockdown in 216 lenvatinib-resistant organoids. \*\*\*\*,  $p < 0.0001$ .
- (H) Scatterplot showing IC<sub>50</sub> change of lenvatinib when treated in combination with veratramine/SR11302/NY2267 (1:1 ratio), respectively, in 216 lenvatinib-resistant organoids. \*\*\*\*,  $p < 0.0001$ .
- (I) A customized chart showing the cumulative sensitivity (labeled on the right) of lenvatinib and veratramine/SR11302/NY2267 combinational treatment in the organoid biobank, at PDO level (upper panel) and patient level (lower panel), represented by the maximum IC<sub>50</sub> value among multi-regional PDOs of a tumor).
- (J) Pathways enriched in genes with significant negative associations with lenvatinib sensitivity. The number of genes identified in a pathway is proportional to the length of a bar, while statistical significance of enrichment (BH-adjusted p value) is indicated by bar color.
- (K) Scatterplot (left panel) showing positive correlation between mRNA levels of c-Jun and  $\beta$ -catenin, and IHC staining of two proteins (right panel) in representative regions (P20C2, P94C2, P20C3, and P94C1).
- (L) Western blotting demonstrating a decrease of c-Jun protein expression upon siRNA-mediated knockdown of  $\beta$ -catenin.
- (M) Dose-response curves of lenvatinib upon  $\beta$ -catenin knockdown (sh  $\beta$ -catenin) in two lenvatinib-resistant organoids (P20C2 and P94C2). Data are representative of at least three independent experiments. Error bars represent means  $\pm$  SD. \*\*\*\*,  $p < 0.0001$ .
- (N) Scatterplot showing IC<sub>50</sub> change of lenvatinib upon  $\beta$ -catenin knockdown in 216 lenvatinib-resistant organoids.  $p < 0.0001$ .
- (O) Dose-response curves of lenvatinib upon overexpression of  $\beta$ -catenin (Flag- $\beta$ -catenin) and mutant  $\beta$ -catenin (S33A/S37A/T41A/S45A) in two lenvatinib-sensitive organoids (P20C3 and P94C1). Data are representative of at least three independent experiments. Error bars represent means  $\pm$  SD. \*\*\*,  $p < 0.001$ .
- (P) Scatterplot (left panel) showing positive correlation between mRNA levels of c-Jun and JNK, and IHC staining of two proteins (right panel) in representative regions (P103C2, P10C1, P103C3, and P10C2).
- (Q) Dose-response curves of lenvatinib upon JNK knockdown (sh JNK) in two lenvatinib-resistant organoids (103C2 and 10C1). Data are representative of at least three independent experiments. Error bars represent means  $\pm$  SD. \*\*\*\*,  $p < 0.0001$ .
- (R) Scatterplot showing IC<sub>50</sub> change of lenvatinib upon JNK knockdown in 216 lenvatinib-resistant organoids. \*\*\*\*,  $p < 0.0001$ .
- (S) Dose-response curves of lenvatinib upon overexpression of JNK (FLAG-JNK) and constitutive active form of JNK (JNKK2-JNK) in two lenvatinib-sensitive organoids (P103C3 and P10C2). See also Figure S5.



(legend on next page)

lenvatinib-resistant organoids (Figure 5R). In contrast, overexpression of wild-type or the constitutive active form of JNK (JNKK2-JNK)<sup>44</sup> in P103C3 and P10C2 organoids significantly reduced lenvatinib sensitivity (Figure 5S). Further, to explore the therapeutic potential of JNK inhibition, we investigated three JNK inhibitors (SP600125, tanzisertib, and JNK-IN-8) in two lenvatinib-resistant organoids (P103C2 and P10C1), which all effectively decreased c-Jun phosphorylation levels (Figure S5G), and sensitized the organoids to lenvatinib treatment (Figure S5H).

Altogether, JNK and Wnt/ $\beta$ -catenin may serve as the upstream regulators of c-Jun in mediating lenvatinib resistance.

### c-Jun inhibition exhibited a marked synergistic effect with lenvatinib via compound PKUF-01 on lenvatinib-resistant organoids

Due to the revealed synergistic effects of lenvatinib and c-Jun inhibition, we designed and synthesized six compounds linking lenvatinib and veratramine (with the best efficacy among three c-Jun inhibitors) (Figures S6A and S6B), which enables targeting the same cancer cells simultaneously for better combinatorial treatment effect. Six compounds were different with the structure of linker  $-(\text{CH}_2)_n-$  or  $-S-S-$ , or the modifications of veratramine in hydrophobic or hydrophilic group. Three lenvatinib-resistant organoids (P20C2, P74C3, and P94C2) were used for comparing efficacies of six compounds (Figure S6C). A compound, designated as PKUF-01 (Figures 6A, S6D, and S6E), can effectively block c-Jun and FGFRs (Figure 6B), and showed promising inhibitory efficacy (Figure 6C). When PKUF-01 was further assessed with the organoid biobank, a significant improvement of sensitivity (represented by decrease in IC<sub>50</sub> values) was shown in comparison with lenvatinib treatment (Figure 6D). Especially, for the 216 lenvatinib-resistant organoids from 90 patients, PKUF-01 induced significant response in 20.0% of these organoids (Figure 6E), which had a marginal increase of 2.9% (20.0% vs. 17.1%) sensitized lenvatinib-resistant organoids compared with co-treatment of two individual agents (veratramine and lenvatinib). The efficacy of PKUF-01 was further examined in organoid-transplant xenograft models. As shown in Figure 6F, treatment with lenvatinib (10 mg/kg IG,

QD) or veratramine (10 mg/kg IG, QD) failed to inhibit the tumor growth in three organoid-derived xenograft models (P20C2, P74C3, and P94C2). In contrast, treatment with PKUF-01 (10 mg/kg IG, QD) significantly inhibited tumor growth.

Moreover, we applied the aforementioned machine-learning-based approach and developed a multi-gene signature for predicting PKUF-01 response. At first, expressions of 205 genes were found with significant associations with PKUF-01 sensitivity, and tumors from TCGA-LIHC dataset could be stratified into four groups using these 205 genes (Figures S6F–S6I). A biomarker consisting of 17 signature genes was then developed, in which c-Jun was also included (Figure 6G). This signature achieved an AUROC of 0.836 in the training set and 0.731 in the validation set (Figure 6H). Additionally, based on GSEA analysis of transcriptome profiles comparing groups of organoids with distinct sensitivity to PKUF-01 treatment (Figure 6I), we found that embryonic organ development-related gene sets and a gene set associated with stem cell<sup>23</sup> (Figure 6J) were up-regulated in the resistant organoids; therefore, targeting stemness might be a potential strategy to overcome the resistance to PKUF-01 treatment.

Last, by analyzing the whole PLC organoid biobank, our results demonstrated that PKUF-01 had a significantly improved efficacy than lenvatinib treatment alone in PLC (54.0% vs. 42.6%), and could benefit 10.4% more PLC patients (34.5% vs. 24.1%) (Figure 6K). Together with seven screened agents used in clinical practice, target therapies could benefit 48.3% PLC patients in total (Figure 6K).

In summary, lenvatinib could target FGFR and other receptors, attenuating downstream signaling to inhibit tumor growth; however, c-Jun, regulated by Wnt/ $\beta$ -catenin and JNK pathways, contributes to lenvatinib resistance. Targeting c-Jun by PKUF-01 showed significant efficacy in lenvatinib-resistant organoids and potentially benefit more PLC patients (Figure 6L).

## DISCUSSION

By development of a large-scale PLC living bank consisting of 399 organoids derived from distinct regions of 144 patient

### Figure 6. A compound PKUF-01 increased the sensitivity of lenvatinib-resistant organoids

- (A) The formula of PKUF-01, linking lenvatinib and veratramine. See Figure S6A for the formulas of all six candidate compounds.
- (B) Western blotting showing the total and phosphorylation level of FGFR, JNK, and c-Jun (veratramine targets) in three lenvatinib-resistant organoids (P20C2, P74C3 and P94C2) upon PKUF-01 treatment.
- (C) Dose-response curves of lenvatinib, veratramine, and PKUF-01 for three lenvatinib-resistant organoids (P20C2, P74C3, and P94C2). Data are representative of at least three independent experiments. Error bars represent means  $\pm$  SD. \*\*\*\*,  $p < 0.0001$ .
- (D) Scatterplot showing IC<sub>50</sub> distribution of lenvatinib and PKUF-01 in all screened 376 organoids.
- (E) Scatterplot showing IC<sub>50</sub> values of lenvatinib and PKUF-01 in 216 lenvatinib-resistant organoids, with gray lines connecting the same organoids. \*\*\*\*,  $p < 0.0001$ .
- (F) Tumor growth curves (upper panels) of three organoid-derived xenografts (P20C2, P74C3, and P94C2) with lenvatinib/veratramine/PKUF-01 treatment alone, or combination treatment of lenvatinib and veratramine. Tumors were imaged after the mice were sacrificed (lower panels). Data are representative of five mice each group. Error bars represent means  $\pm$  SD. \*,  $p < 0.05$ ; \*\*\*,  $p < 0.001$ ; ns, not significant. However, due to a limited intragastric absorption of PKUF-01 by oral administration, there was no significant difference shown between PKUF-01 and the combined treatment (lenvatinib and veratramine) for *in vivo* models.
- (G) Bar plot showing expression correlations with drug sensitivity for 17 signature genes predicting PKUF-01 response.
- (H) ROC curves of the 17-gene signature predicting PKUF-01 response in the training ( $n = 106$ ) and validation ( $n = 106$ ) sets. Area under ROC curves (AUROCs) are indicated.
- (I) GSEA enrichment plot showing the selected gene sets significantly changed in lenvatinib-resistant organoids that PKUF-01 failed to sensitize.
- (J) GSEA enrichment plot for a gene set associated with stem cell<sup>23</sup> using the same group comparison as (H).
- (K) A customized chart showing the cumulative sensitivity (labeled on the right) of seven approved targeted drugs and PKUF-01 in the organoid biobank, at PDO level (upper panel) and patient level (lower panel).
- (L) The proposed model of c-Jun-mediated lenvatinib resistance. See also Figure S6.

tumors, we recapitulated a full spectrum of inter- and intra-tumor heterogeneity of liver cancer *ex vivo*, enabling a comprehensive investigation integrating genomic profiles and functional and clinical phenotypes. PLC patients with high levels of mutation/CNA ITH were found to be associated with worse survival, and being more resistant to lenvatinib treatment. Using machine learning approaches, we modeled pharmacogenomic interactions of clinically relevant drugs in PLC and developed robust multi-gene expression signatures predicting sensitivity to treatment of anti-angiogenic tyrosine kinase inhibitors (lenvatinib, sorafenib, regorafenib, and apatinib), respectively, which were in agreement with clinical responses from patients, warranting further investigation to guide clinical decision. Together with Liver Cancer Model Repository,<sup>45</sup> a study characterized by the pharmacogenomic landscape of human liver cell line models, we both identified the significant association of WNT signaling activity with sorafenib response. In addition, within lenvatinib signature genes, we identified a key role of c-Jun in mediating lenvatinib resistance through JNK and  $\beta$ -catenin signaling, and synthesized a compound PKUF-01, demonstrating a marked synergistic effect between veratramine (c-Jun inhibitor) and lenvatinib. These findings may be linked with a recent study showing anti-proliferative effects by combination of gefitinib (EGFR inhibitor) and lenvatinib in HCC, as c-Jun was indicated as a downstream gene regulated by EGFR signaling,<sup>46</sup> which needs further investigation to illustrate the exact mechanism.

In addition, the combination of immune checkpoint inhibitors (ICIs) with anti-angiogenic tyrosine kinase inhibitors (TKIs) or antibodies has been indicated with the capability to drive immune cell infiltration into immune cold tumors through vascular normalization,<sup>47</sup> which promoted the FDA approval for the regimen of atezolizumab plus bevacizumab in HCC, and several multi-center phase 3 clinical trials (NCT03713593, NCT04194775, NCT04770896, NCT04246177, NCT04777851) with different combinations of ICI and anti-angiogenic TKI. Our developed predictive signatures for anti-angiogenic TKI may also aid better stratification to identify patients benefiting from the combination therapy, with TMB considered simultaneously. Further clinical validation could be essentially valuable, as the LEAP-002 study (NCT03713593) investigating the combination of lenvatinib plus pembrolizumab recently missed its dual primary endpoints in patients with unresectable HCC.<sup>48</sup>

Together, our study provides a valuable resource to characterize the influence of genomic heterogeneity on the sensitivity to different therapeutic agents. The predictive biomarkers for anti-angiogenic TKIs and the combination treatment option that we developed warrant future clinical investigation to accelerate precision medicine in liver cancer.

## STAR★METHODS

Detailed methods are provided in the online version of this paper and include the following:

- KEY RESOURCES TABLE
- RESOURCE AVAILABILITY

- Lead contact
- Materials availability
- Data and code availability

## ● EXPERIMENTAL MODELS AND STUDY PARTICIPANT DETAILS

- Sample collection and patient information
- Tissue dissociation and organoid culturing
- Organoid-derived tumor xenograft

## ● METHOD DETAILS

- Histology and immunostaining
- WES sequencing and data pre-processing
- Somatic mutation calling
- Copy number calling
- Phylogenetic tree
- RNA-seq and quantification
- Drug screening
- Differential gene expression and gene set enrichment analysis
- Machine learning model of drug response
- Plasmids and transfection
- Synthesis of PKUF-01

## ● QUANTIFICATION AND STATISTICAL ANALYSES

## SUPPLEMENTAL INFORMATION

Supplemental information can be found online at <https://doi.org/10.1016/j.ccell.2024.03.004>.

## ACKNOWLEDGMENTS

We would like to thank all patients who generously donated tissue. This work was supported by grants from the National Natural Science Foundation of China (No. 82030079, 81972656, 82341005 and 81988101 for N.Z.), the National Science and Technology Major Project of China (2022YFC3400900 for N.Z.), Baidu Foundation of China (No. 2020BD015 for N.Z.), the National Natural Science Foundation of China (No. 82273253 for J.W., No. 82003187 for H.Y., and No. 81902477 for H.Z.), Baidu Foundation of China (No. 2019BD012 for J.W.), Beijing Municipal Science and Technology Commission (Z20110008320006 for J.W.), Science and Technology Development Foundation of Henan Province (No. 212102310135 for F.H.), and Henan Province Young Scientist Project (No. 225200810086 for H.Z.) We also thank Xinxia Tian and Jing Wu for technical assistance in pathology and IF staining.

## AUTHOR CONTRIBUTIONS

N.Z., J.W., and J.Z. supervised all of the research. H.Y. established the organoid biobank. J.C. and J.W. performed genomic analyses and implemented the machine learning models. H.Z. and J.Z. collected most samples and clinical information. Y.Y., H.Q., Y.L., F.H., and N.Y. provided additional clinical samples. H.Y., Y.W., and T.Z. performed experiments. H.X. and X.Y. synthesized PKUF-01. J.W. and L.C. designed the machine learning models and interpreted the analysis results. N.Z., J.W., H.Y., and J.C. wrote the manuscript. N.Z., J.W., H.Y., J.C., and R.L. revised the manuscript. All authors commented on the manuscript.

## DECLARATION OF INTERESTS

The authors declare no competing interests.

Received: January 12, 2023  
Revised: December 27, 2023  
Accepted: March 11, 2024  
Published: April 8, 2024

REFERENCES

- Sung, H., Ferlay, J., Siegel, R.L., Laversanne, M., Soerjomataram, I., Jemal, A., and Bray, F. (2021). Global Cancer Statistics 2020: GLOBOCAN Estimates of Incidence and Mortality Worldwide for 36 Cancers in 185 Countries. *CA. Cancer J. Clin.* 71, 209–249.
- Sia, D., Villanueva, A., Friedman, S.L., and Llovet, J.M. (2017). Liver Cancer Cell of Origin, Molecular Class, and Effects on Patient Prognosis. *Gastroenterology* 152, 745–761.
- Seehawer, M., D'Artista, L., and Zender, L. (2019). The Worst from Both Worlds: cHCC-ICC. *Cancer Cell* 35, 823–824.
- Paradis, V., and Zucman-Rossi, J. (2022). Pathogenesis of primary liver carcinomas. *J. Hepatol.* 78, 448–449.
- Llovet, J.M., Kelley, R.K., Villanueva, A., Singal, A.G., Pikarsky, E., Roayaie, S., Lencioni, R., Koike, K., Zucman-Rossi, J., and Finn, R.S. (2021). Hepatocellular carcinoma. *Nat. Rev. Dis. Primers* 7, 6.
- Kudo, M., Finn, R.S., Qin, S., Han, K.H., Ikeda, K., Piscaglia, F., Baron, A., Park, J.W., Han, G., Jassem, J., et al. (2018). Lenvatinib versus sorafenib in first-line treatment of patients with unresectable hepatocellular carcinoma: a randomised phase 3 non-inferiority trial. *Lancet* 391, 1163–1173.
- Bruix, J., Qin, S., Merle, P., Granito, A., Huang, Y.H., Bodoky, G., Pracht, M., Yokosuka, O., Rosmorduc, O., Breder, V., et al. (2017). Regorafenib for patients with hepatocellular carcinoma who progressed on sorafenib treatment (RESORCE): a randomised, double-blind, placebo-controlled, phase 3 trial. *Lancet* 389, 56–66.
- Qin, S., Li, Q., Gu, S., Chen, X., Lin, L., Wang, Z., Xu, A., Chen, X., Zhou, C., Ren, Z., et al. (2021). Apatinib as second-line or later therapy in patients with advanced hepatocellular carcinoma (AHELP): a multicentre, double-blind, randomised, placebo-controlled, phase 3 trial. *Lancet. Gastroenterol. Hepatol.* 6, 559–568.
- Li, X., Ramadori, P., Pfister, D., Seehawer, M., Zender, L., and Heikenwalder, M. (2021). The immunological and metabolic landscape in primary and metastatic liver cancer. *Nat. Rev. Cancer* 21, 541–557.
- Dagogo-Jack, I., and Shaw, A.T. (2018). Tumour heterogeneity and resistance to cancer therapies. *Nat. Rev. Clin. Oncol.* 15, 81–94.
- Chaisaingmongkol, J., Budhu, A., Dang, H., Rabibhadana, S., Pupacdi, B., Kwon, S.M., Forgues, M., Pomyen, Y., Bhudhisawasdi, V., Lertprasertsuke, N., et al. (2017). Common Molecular Subtypes Among Asian Hepatocellular Carcinoma and Cholangiocarcinoma. *Cancer Cell* 32, 57–70.e3.
- Xue, R., Li, R., Guo, H., Guo, L., Su, Z., Ni, X., Qi, L., Zhang, T., Li, Q., Zhang, Z., et al. (2016). Variable Intra-Tumor Genomic Heterogeneity of Multiple Lesions in Patients With Hepatocellular Carcinoma. *Gastroenterology* 150, 998–1008.
- Xiang, X., Liu, Z., Zhang, C., Li, Z., Gao, J., Zhang, C., Cao, Q., Cheng, J., Liu, H., Chen, D., et al. (2021). IDH Mutation Subgroup Status Associates with Intratumor Heterogeneity and the Tumor Microenvironment in Intrahepatic Cholangiocarcinoma. *Adv. Sci.* 8, e2101230.
- Dong, L., Lu, D., Chen, R., Lin, Y., Zhu, H., Zhang, Z., Cai, S., Cui, P., Song, G., Rao, D., et al. (2022). Proteogenomic characterization identifies clinically relevant subgroups of intrahepatic cholangiocarcinoma. *Cancer Cell* 40, 70–87.e15.
- Xue, R., Chen, L., Zhang, C., Fujita, M., Li, R., Yan, S.M., Ong, C.K., Liao, X., Gao, Q., Sasagawa, S., et al. (2019). Genomic and Transcriptomic Profiling of Combined Hepatocellular and Intrahepatic Cholangiocarcinoma Reveals Distinct Molecular Subtypes. *Cancer Cell* 35, 932–947.e8.
- Duan, M., Hao, J., Cui, S., Worthley, D.L., Zhang, S., Wang, Z., Shi, J., Liu, L., Wang, X., Ke, A., et al. (2018). Diverse modes of clonal evolution in HBV-related hepatocellular carcinoma revealed by single-cell genome sequencing. *Cell Res.* 28, 359–373.
- Gao, Q., Wang, Z.C., Duan, M., Lin, Y.H., Zhou, X.Y., Worthley, D.L., Wang, X.Y., Niu, G., Xia, Y., Deng, M., et al. (2017). Cell Culture System for Analysis of Genetic Heterogeneity Within Hepatocellular Carcinomas and Response to Pharmacologic Agents. *Gastroenterology* 152, 232–242.e4.
- Vitale, I., Shema, E., Loi, S., and Galluzzi, L. (2021). Intratumoral heterogeneity in cancer progression and response to immunotherapy. *Nat. Med.* 27, 212–224.
- Lee, S.H., Hu, W., Matulay, J.T., Silva, M.V., Owczarek, T.B., Kim, K., Chua, C.W., Barlow, L.J., Kandoth, C., Williams, A.B., et al. (2018). Tumor Evolution and Drug Response in Patient-Derived Organoid Models of Bladder Cancer. *Cell* 173, 515–528.e17.
- Vlachogiannis, G., Hedayat, S., Vatsiou, A., Jamin, Y., Fernández-Mateos, J., Khan, K., Lampis, A., Eason, K., Huntingford, I., Burke, R., et al. (2018). Patient-derived organoids model treatment response of metastatic gastrointestinal cancers. *Science* 359, 920–926.
- Kopper, O., de Witte, C.J., Löhmussaar, K., Valle-Inclán, J.E., Hami, N., Kester, L., Balgobind, A.V., Korving, J., Proost, N., Begthel, H., et al. (2019). An organoid platform for ovarian cancer captures intra- and inter-patient heterogeneity. *Nat. Med.* 25, 838–849.
- Jacob, F., Salinas, R.D., Zhang, D.Y., Nguyen, P.T.T., Schnoll, J.G., Wong, S.Z.H., Thokala, R., Sheikh, S., Saxena, D., Prokop, S., et al. (2020). A Patient-Derived Glioblastoma Organoid Model and Biobank Recapitulates Inter- and Intra-tumoral Heterogeneity. *Cell* 180, 188–204.e22.
- Broutier, L., Mastrogianni, G., Versteegen, M.M., Francies, H.E., Gavarró, L.M., Bradshaw, C.R., Allen, G.E., Arnes-Benito, R., Sidorova, O., Gaspersz, M.P., et al. (2017). Human primary liver cancer-derived organoid cultures for disease modeling and drug screening. *Nat. Med.* 23, 1424–1435.
- Nuciforo, S., Fofana, I., Matter, M.S., Blumer, T., Calabrese, D., Boldanova, T., Piscuoglio, S., Wieland, S., Ringnald, F., Schwank, G., et al. (2018). Organoid Models of Human Liver Cancers Derived from Tumor Needle Biopsies. *Cell Rep.* 24, 1363–1376.
- Li, L., Knutsdottir, H., Hui, K., Weiss, M.J., He, J., Philoppe, B., Cameron, A.M., Wolfgang, C.L., Pawlik, T.M., Ghiaur, G., et al. (2019). Human primary liver cancer organoids reveal intratumor and interpatient drug response heterogeneity. *JCI Insight* 4, e121490.
- Zhao, Y., Li, Z.X., Zhu, Y.J., Fu, J., Zhao, X.F., Zhang, Y.N., Wang, S., Wu, J.M., Wang, K.T., Wu, R., et al. (2021). Single-Cell Transcriptome Analysis Uncovers Intratumoral Heterogeneity and Underlying Mechanisms for Drug Resistance in Hepatobiliary Tumor Organoids. *Adv. Sci.* 8, e2003897.
- Wang, W., Yuan, T., Ma, L., Zhu, Y., Bao, J., Zhao, X., Zhao, Y., Zong, Y., Zhang, Y., Yang, S., et al. (2022). Hepatobiliary Tumor Organoids Reveal HLA Class I Neoantigen Landscape and Antitumoral Activity of Neoantigen Peptide Enhanced with Immune Checkpoint Inhibitors. *Adv. Sci.* 9, e2105810.
- van Tienderen, G.S., Li, L., Broutier, L., Saito, Y., Inacio, P., Huch, M., Selaru, F.M., van der Laan, L.J.W., and Versteegen, M.M.A. (2022). Hepatobiliary tumor organoids for personalized medicine: a multicenter view on establishment, limitations, and future directions. *Cancer Cell* 40, 226–230.
- Hoshida, Y., Nijman, S.M.B., Kobayashi, M., Chan, J.A., Brunet, J.P., Chiang, D.Y., Villanueva, A., Newell, P., Ikeda, K., Hashimoto, M., et al. (2009). Integrative transcriptome analysis reveals common molecular subclasses of human hepatocellular carcinoma. *Cancer Res.* 69, 7385–7392.
- Torrecilla, S., Sia, D., Harrington, A.N., Zhang, Z., Cabellos, L., Cornella, H., Moeini, A., Camprecios, G., Leow, W.Q., Fiel, M.I., et al. (2017). Trunk mutational events present minimal intra- and inter-tumoral heterogeneity in hepatocellular carcinoma. *J. Hepatol.* 67, 1222–1231.
- Cheng, A.L., Qin, S., Ikeda, M., Galle, P.R., Ducreux, M., Kim, T.Y., Lim, H.Y., Kudo, M., Breder, V., Merle, P., et al. (2022). Updated efficacy and safety data from IMbrave150: Atezolizumab plus bevacizumab vs.

- sorafenib for unresectable hepatocellular carcinoma. *J. Hepatol.* **76**, 862–873.
32. Silverman, I.M., Hollebecque, A., Friboulet, L., Owens, S., Newton, R.C., Zhen, H., Féliz, L., Zecchetto, C., Melisi, D., and Burn, T.C. (2021). Clinicogenomic Analysis of FGFR2-Rearranged Cholangiocarcinoma Identifies Correlates of Response and Mechanisms of Resistance to Pemigatinib. *Cancer Discov.* **11**, 326–339.
  33. Abou-Alfa, G.K., Macarulla, T., Javle, M.M., Kelley, R.K., Lubner, S.J., Adeva, J., Cleary, J.M., Catenacci, D.V., Borad, M.J., Bridgewater, J., et al. (2020). Ivosidenib in IDH1-mutant, chemotherapy-refractory cholangiocarcinoma (ClarIDHy): a multicentre, randomised, double-blind, placebo-controlled, phase 3 study. *Lancet Oncol.* **21**, 796–807.
  34. Kelley, R.K., Ueno, M., Yoo, C., Finn, R.S., Furuse, J., Ren, Z., Yau, T., Klumpen, H.J., Chan, S.L., Ozaka, M., et al. (2023). Pembrolizumab in combination with gemcitabine and cisplatin compared with gemcitabine and cisplatin alone for patients with advanced biliary tract cancer (KEYNOTE-966): a randomised, double-blind, placebo-controlled, phase 3 trial. *Lancet* **401**, 1853–1865.
  35. McGranahan, N., and Swanton, C. (2017). Clonal Heterogeneity and Tumor Evolution: Past, Present, and the Future. *Cell* **168**, 613–628.
  36. Jerby-Aronn, L., Shah, P., Cuoco, M.S., Rodman, C., Su, M.J., Melms, J.C., Leeson, R., Kanodia, A., Mei, S., Lin, J.R., et al. (2018). A Cancer Cell Program Promotes T Cell Exclusion and Resistance to Checkpoint Blockade. *Cell* **175**, 984–997.e24.
  37. Sammut, S.J., Crispin-Ortuzar, M., Chin, S.F., Provenzano, E., Bardwell, H.A., Ma, W., Cope, W., Dariush, A., Dawson, S.J., Abraham, J.E., et al. (2022). Multi-omic machine learning predictor of breast cancer therapy response. *Nature* **601**, 623–629.
  38. Uhlén, M., Fagerberg, L., Hallström, B.M., Lindskog, C., Oksvold, P., Mardinoglu, A., Sivertsson, Å., Kampf, C., Sjöstedt, E., Asplund, A., et al. (2015). Proteomics. Tissue-based map of the human proteome. *Science* **347**, 1260419.
  39. Network, C.G.A.R. (2017). Comprehensive and Integrative Genomic Characterization of Hepatocellular Carcinoma. *Cell* **169**, 1327–1341.e3.
  40. Lu, Y., Shen, H., Huang, W., He, S., Chen, J., Zhang, D., Shen, Y., and Sun, Y. (2021). Genome-scale CRISPR-Cas9 knockout screening in hepatocellular carcinoma with lenvatinib resistance. *Cell Death Discov.* **7**, 359.
  41. Jin, H., Shi, Y., Lv, Y., Yuan, S., Ramirez, C.F.A., Liefink, C., Wang, L., Wang, S., Wang, C., Dias, M.H., et al. (2021). EGFR activation limits the response of liver cancer to lenvatinib. *Nature* **595**, 730–734.
  42. Zucman-Rossi, J., Benhamouche, S., Godard, C., Boyault, S., Grimber, G., Balabaud, C., Cunha, A.S., Bioulac-Sage, P., and Perret, C. (2007). Differential effects of inactivated Axin1 and activated beta-catenin mutations in human hepatocellular carcinomas. *Oncogene* **26**, 774–780.
  43. Perugorria, M.J., Olaizola, P., Labiano, I., Esparza-Baquer, A., Marzioni, M., Marin, J.J.G., Bujanda, L., and Banales, J.M. (2019). Wnt-beta-catenin signalling in liver development, health and disease. *Nat. Rev. Gastroenterol. Hepatol.* **16**, 121–136.
  44. Zheng, C., Xiang, J., Hunter, T., and Lin, A. (1999). The JNKK2-JNK1 fusion protein acts as a constitutively active c-Jun kinase that stimulates c-Jun transcription activity. *J. Biol. Chem.* **274**, 28966–28971.
  45. Qiu, Z., Li, H., Zhang, Z., Zhu, Z., He, S., Wang, X., Wang, P., Qin, J., Zhuang, L., Wang, W., et al. (2019). A Pharmacogenomic Landscape in Human Liver Cancers. *Cancer Cell* **36**, 179–193.e11.
  46. Ma, G., Liang, Y., Chen, Y., Wang, L., Li, D., Liang, Z., Wang, X., Tian, D., Yang, X., and Niu, H. (2020). Glutamine Deprivation Induces PD-L1 Expression via Activation of EGFR/ERK/c-Jun Signaling in Renal Cancer. *Mol. Cancer Res.* **18**, 324–339.
  47. Llovet, J.M., Castet, F., Heikenwalder, M., Maini, M.K., Mazzaferro, V., Pinato, D.J., Pikarsky, E., Zhu, A.X., and Finn, R.S. (2022). Immunotherapies for hepatocellular carcinoma. *Nat. Rev. Clin. Oncol.* **19**, 151–172.
  48. Finn, R.S., Kudo, M., Merle, P., Meyer, T., Qin, S., Ikeda, M., Xu, R., Edeline, J., Ryoo, B.-Y., Ren, Z., et al. (2022). LBA34 Primary results from the phase III LEAP-002 study: Lenvatinib plus pembrolizumab versus lenvatinib as first-line (1L) therapy for advanced hepatocellular carcinoma (aHCC). *ESMO* **33**, S1401.
  49. Li, H., and Durbin, R. (2009). Fast and accurate short read alignment with Burrows-Wheeler transform. *Bioinformatics* **25**, 1754–1760.
  50. McKenna, A., Hanna, M., Banks, E., Sivachenko, A., Cibulskis, K., Kernysky, A., Garimella, K., Altshuler, D., Gabriel, S., Daly, M., and DePristo, M.A. (2010). The Genome Analysis Toolkit: a MapReduce framework for analyzing next-generation DNA sequencing data. *Genome Res.* **20**, 1297–1303.
  51. Wang, K., Li, M., and Hakonarson, H. (2010). ANNOVAR: functional annotation of genetic variants from high-throughput sequencing data. *Nucleic Acids Res.* **38**, e164.
  52. Talevich, E., Shain, A.H., Botton, T., and Bastian, B.C. (2016). CNVkit: Genome-Wide Copy Number Detection and Visualization from Targeted DNA Sequencing. *PLoS Comput. Biol.* **12**, e1004873.
  53. Mermel, C.H., Schumacher, S.E., Hill, B., Meyerson, M.L., Beroukhi, R., and Getz, G. (2011). GISTIC2.0 facilitates sensitive and confident localization of the targets of focal somatic copy-number alteration in human cancers. *Genome Biol.* **12**, R41.
  54. Cibulskis, K., Lawrence, M.S., Carter, S.L., Sivachenko, A., Jaffe, D., Sougnez, C., Gabriel, S., Meyerson, M., Lander, E.S., and Getz, G. (2013). Sensitive detection of somatic point mutations in impure and heterogeneous cancer samples. *Nat. Biotechnol.* **31**, 213–219.
  55. Tamura, K., Peterson, D., Peterson, N., Stecher, G., Nei, M., and Kumar, S. (2011). MEGA5: molecular evolutionary genetics analysis using maximum likelihood, evolutionary distance, and maximum parsimony methods. *Mol. Biol. Evol.* **28**, 2731–2739.
  56. Dobin, A., Davis, C.A., Schlesinger, F., Drenkow, J., Zaleski, C., Jha, S., Batut, P., Chaisson, M., and Gingeras, T.R. (2013). STAR: ultrafast universal RNA-seq aligner. *Bioinformatics* **29**, 15–21.
  57. Anders, S., Pyl, P.T., and Huber, W. (2015). HTSeq—a Python framework to work with high-throughput sequencing data. *Bioinformatics* **31**, 166–169.
  58. Li, B., and Dewey, C.N. (2011). RSEM: accurate transcript quantification from RNA-Seq data with or without a reference genome. *BMC Bioinf.* **12**, 323.
  59. Subramanian, A., Tamayo, P., Mootha, V.K., Mukherjee, S., Ebert, B.L., Gillette, M.A., Paulovich, A., Pomeroy, S.L., Golub, T.R., Lander, E.S., and Mesirov, J.P. (2005). Gene set enrichment analysis: a knowledge-based approach for interpreting genome-wide expression profiles. *Proc. Natl. Acad. Sci. USA* **102**, 15545–15550.
  60. Yu, G., Wang, L.G., Han, Y., and He, Q.Y. (2012). clusterProfiler: an R package for comparing biological themes among gene clusters. *OMICS* **16**, 284–287.
  61. Love, M.I., Huber, W., and Anders, S. (2014). Moderated estimation of fold change and dispersion for RNA-seq data with DESeq2. *Genome Biol.* **15**, 550.
  62. Llovet, J.M., and Lencioni, R. (2020). mRECIST for HCC: Performance and novel refinements. *J. Hepatol.* **72**, 288–306.
  63. Eisenberg, E., and Levanon, E.Y. (2013). Human housekeeping genes, revisited. *Trends Genet.* **29**, 569–574.
  64. Chen, P., Zhang, X., Ding, R., Yang, L., Lyu, X., Zeng, J., Lei, J.H., Wang, L., Bi, J., Shao, N., et al. (2021). Patient-Derived Organoids Can Guide Personalized-Therapies for Patients with Advanced Breast Cancer. *Adv. Sci.* **8**, e2101176.
  65. Ganesh, K., Wu, C., O'Rourke, K.P., Szeglin, B.C., Zheng, Y., Sauvé, C.E.G., Adileh, M., Wasserman, I., Marco, M.R., Kim, A.S., et al. (2019). A rectal cancer organoid platform to study individual responses to chemotherapy. *Nat. Med.* **25**, 1607–1614.

66. Mei, K., Qin, S., Chen, Z., Liu, Y., Wang, L., and Zou, J. (2021). Camrelizumab in combination with apatinib in second-line or above therapy for advanced primary liver cancer: cohort A report in a multicenter phase Ib/II trial. *J. Immunother. Cancer* 9, e002191.
67. Cremolini, C., Antoniotti, C., Stein, A., Bendell, J., Gruenberger, T., Rossini, D., Masi, G., Ongaro, E., Hurwitz, H., Falcone, A., et al. (2020). Individual Patient Data Meta-Analysis of FOLFOXIRI Plus Bevacizumab Versus Doublets Plus Bevacizumab as Initial Therapy of Unresectable Metastatic Colorectal Cancer. *J. Clin. Oncol.* JCO2001225.
68. Zhao, T., Cao, L., Ji, J., Chang, D.K., and Wu, J. (2023). ReProMSig: an integrative platform for development and application of reproducible multivariable models for cancer prognosis supporting guideline-based transparent reporting. *Brief. Bioinform.* 24, bbad267.
69. Broutier, L., Andersson-Rolf, A., Hindley, C.J., Boj, S.F., Clevers, H., Koo, B.K., and Huch, M. (2016). Culture and establishment of self-renewing human and mouse adult liver and pancreas 3D organoids and their genetic manipulation. *Nat. Protoc.* 11, 1724–1743.

## STAR★METHODS

### KEY RESOURCES TABLE

REAGENT or RESOURCE	SOURCE	IDENTIFIER
<b>Antibodies</b>		
HepPar1 antibody	Abcam	Cat# ab190706; RRID: AB_3095623
AFP antibody	Abcam	Cat#ab46799; RRID: AB_867622
KRT19 antibody	Abcam	Cat#EP1580Y; RRID: AB_1192460
EPCAM antibody	Abcam	Cat#ab223582; RRID: AB_2762366
c-JUN antibody	Abcam	Cat#ab40766; RRID: AB_731602
JNK antibody	Abcam	Cat#ab199380; RRID: AB_3095624
β-catenin antibody	Abcam	Cat#ab32572; RRID: AB_725966
Ser63 of c-Jun antibody	Abcam	Cat# ab32385; RRID: AB_726900
Ser73 of c-Jun antibody	Abcam	Cat# ab30620; RRID: AB_726902
Thr91 of c-Jun antibody	Abcam	Cat# ab81319; RRID: AB_1640354
Thr93 of c-Jun antibody	Abcam	Cat# ab79756; RRID: AB_1603343
FGFR1 antibody	Abcam	Cat# ab76464; RRID: AB_1523613
Y653 of FGFR1 antibody	Abcam	Cat# ab173305; RRID: AB_3094883
Y654 of FGFR1 antibody	Abcam	Cat# ab59194; RRID: AB_941585
FGFR2 antibody	Abcam	Cat# ab109372; RRID: AB_2934131
Y769 of FGFR2 antibody	Absin	Cat# abs139977
S782 of FGFR2 antibody	Absin	Cat# abs140266
FGFR3 antibody	Abcam	Cat# ab133644; RRID: AB_2810262
Y724 of FGFR3 antibody	Abcam	Cat# ab155960; RRID: AB_3095625
FGFR4 antibody	Abcam	Cat# ab44971; RRID: AB_732374
Y642 of FGFR4 antibody	Abcam	Cat# ab192589; RRID: AB_3095628
JNK antibody	Abcam	Cat#ab199380; RRID: AB_3095624
T183/Y185 of JNK antibody	Abcam	Cat#ab76572; RRID: AB_1523840
<b>Biological samples</b>		
Human liver cancer tissue	This study	<a href="#">Table S1</a>
<b>Chemicals, peptides and recombinant proteins</b>		
Sorafenib	MCE	Cat#HY-10201
Lenvatinib	MCE	Cat#HY-10981
Regorafenib	MCE	Cat#HY-10331
Apatinib	Selleck	Cat#S5248
Bevacizumab	MCE	Cat#HY-P9906
Pemigatinib	MCE	Cat#HY-109099
Ivosidenib	MCE	Cat#HY-18767
Gemcitabine	MCE	Cat#LY 188011
Cisplatin	MCE	Cat#HY-17394
Veratramine	MCE	Cat#HY-N0837
SR11302	MCE	Cat#HY-15870
NY2267	MCE	Cat#HY-134975
PKUF-01	This study	N/A
SP600125	Selleck	Cat# S1460
Tanzisertib (CC-930)	Selleck	Cat# S8490
JNK-IN-8	Selleck	Cat# S4901
Advanced DMEM/F12	Corning	Cat#10-092-CVRC
Penicillin/streptomycin	Gibco	Cat#15140122

(Continued on next page)

<b>Continued</b>		
REAGENT or RESOURCE	SOURCE	IDENTIFIER
Glutamax	Gibco	Cat#35050061
HEPES	Tocris	Cat#3173
B27 supplement (without vitamin A)	Life	Cat#12587-010
N2 supplement	Life	Cat#17502048
N-acetyl-L-cysteine	Sigma	Cat#A9165-5g
Nicotinamide	Sigma	Cat#N0636
Recombinant human (Leu15)-gastrin I	Meilunbio	Cat#MB10217
Recombinant human EGF	Peprtech	Cat#AF-100-15
Recombinant human FGF10	Peprtech	Cat#100-26
Recombinant human HGF	Peprtech	Cat#100-39
Forskolin	Tocris Bioscience	Cat#1099/10
A83-01	Abmole	Cat#M5037
Y27632	Sigma-Aldrich	Cat#Y0503-1MG
Recombinant human Noggin	Peprtech	Cat#120-10C
Rspo-1	Novoprotein	Cat#CX83
Wnt3a	SAB	Cat#AP72293-2
Matrigel	Corning	Cat#356231
<b>Critical commercial assays</b>		
DNeasy & RNeasy isolation kit	Qiagen	Cat#80204
CCK-8 Cell Viability Assay	Beyotime	Cat#C0040
<b>Deposited data</b>		
Bulk RNA-seq data	This paper	GSA: HRA006499
Bulk WES data	This paper	GSA: HRA006499
TCGA LIHC data	Cancer Genome Atlas Research Network <sup>39</sup>	<a href="https://xena.ucsc.edu">https://xena.ucsc.edu</a>
Mendeley Dataset 1: Transcriptome quantification of bulk RNA-seq data	This paper	Mendeley Data: <a href="http://www.doi.org/10.17632/rv2w3dv9rs.2">http://www.doi.org/10.17632/rv2w3dv9rs.2</a>
Mendeley Dataset 2: IF and IHC staining in <a href="#">Figures 1D</a> and <a href="#">Data S1.3</a>	This paper	Mendeley Data: <a href="http://www.doi.org/10.17632/mp5ncd4z93.4">http://www.doi.org/10.17632/mp5ncd4z93.4</a>
<b>Experimental models: Cell lines</b>		
Liver cancer organoid lines	This study	<a href="#">Tables S1</a>
<b>Experimental models: Organisms/strains</b>		
Balb/c nude mice	Peking University First Hospital	<a href="https://www.pkufh.com/Html/News/Articles/13312.html">https://www.pkufh.com/Html/News/Articles/13312.html</a>
<b>Recombinant DNA</b>		
Flag c-JUN vector	Mailgene biosciences	F2807
Flag $\beta$ -catenin vector	Mailgene biosciences	F5300
Flag JNK vector	Mailgene biosciences	F5156
sh c-JUN vector	GenePharma	C01001
sh $\beta$ -catenin vector	Mailgene biosciences	F3927
sh JNK vector	Mailgene biosciences	G1290
Mutant $\beta$ -catenin vector S33A	Mailgene biosciences	K8525
Mutant $\beta$ -catenin vector S37A	Mailgene biosciences	K8527
Mutant $\beta$ -catenin vector T41A	Mailgene biosciences	K8529
Mutant $\beta$ -catenin vector S45A	Mailgene biosciences	K8531
Constitutive active JNK vector	Mailgene biosciences	E2547
<b>Software and algorithms</b>		
Bwa-mem2 (v2.0)	Li and Durbin <sup>49</sup>	<a href="https://github.com/bwa-mem2/bwa-mem2">https://github.com/bwa-mem2/bwa-mem2</a>

(Continued on next page)

**Continued**

REAGENT or RESOURCE	SOURCE	IDENTIFIER
GATK (v4.1.2.0)	McKenna et al. <sup>50</sup>	<a href="https://software.broadinstitute.org/gatk/download">https://software.broadinstitute.org/gatk/download</a>
ANNOVAR (version date 2019-10)	Wang et al. <sup>51</sup>	<a href="http://annovar.openbioinformatics.org/en/latest">http://annovar.openbioinformatics.org/en/latest</a>
CNVkit (v0.9.7.b1)	Talevich et al. <sup>52</sup>	<a href="https://github.com/etal/cnvkit">https://github.com/etal/cnvkit</a>
GISTIC (v2.0)	Mermel et al. <sup>53</sup>	<a href="https://software.broadinstitute.org/cancer/cga/gistic">https://software.broadinstitute.org/cancer/cga/gistic</a>
MuTect (v2.0)	Cibulskis et al. <sup>54</sup>	wrapped in GATK
MEGA5	Tamura et al. <sup>55</sup>	<a href="https://www.megasoftware.net">https://www.megasoftware.net</a>
STAR (v2.7.3a)	Dobin et al. <sup>56</sup>	<a href="https://github.com/alexdobin/STAR">https://github.com/alexdobin/STAR</a>
HTSeq (v0.12.4)	Anders et al. <sup>57</sup>	<a href="https://htseq.readthedocs.io">https://htseq.readthedocs.io</a>
RSEM (v1.3.3)	Li and Dewey <sup>58</sup>	<a href="http://deweylab.github.io/RSEM">http://deweylab.github.io/RSEM</a>
GSEA	Subramanian et al. <sup>59</sup>	<a href="https://www.gsea-msigdb.org/gsea">https://www.gsea-msigdb.org/gsea</a>
ClusterProfiler (v3.14.3)	Yu et al. <sup>60</sup>	<a href="https://bioconductor.org/packages/release/bioc/html/clusterProfiler.html">https://bioconductor.org/packages/release/bioc/html/clusterProfiler.html</a>
DESeq2 (v1.24.0)	Love et al. <sup>61</sup>	<a href="https://bioconductor.org/packages/release/bioc/html/DESeq2.html">https://bioconductor.org/packages/release/bioc/html/DESeq2.html</a>
R (v4.0.3)	CRAN	<a href="https://cran.r-project.org/">https://cran.r-project.org/</a>
stats	CRAN	<a href="https://r-project.org/web/packages/stats">https://r-project.org/web/packages/stats</a>
survival	CRAN	<a href="https://cran.r-project.org/web/packages/survival/index.html">https://cran.r-project.org/web/packages/survival/index.html</a>
ROCR	CRAN	<a href="https://cran.r-project.org/web/packages/ROCR/index.html">https://cran.r-project.org/web/packages/ROCR/index.html</a>
Bootstrap	CRAN	<a href="https://cran.r-project.org/web/packages/bootstrap/index.html">https://cran.r-project.org/web/packages/bootstrap/index.html</a>
glmnet	CRAN	<a href="https://cran.r-project.org/web/packages/glmnet/index.html">https://cran.r-project.org/web/packages/glmnet/index.html</a>
Complexheatmap	Bioconductor	<a href="https://bioconductor.org/packages/release/bioc/html/ComplexHeatmap.html">https://bioconductor.org/packages/release/bioc/html/ComplexHeatmap.html</a>
pheatmap	CRAN	<a href="https://cran.r-project.org/web/packages/pheatmap">https://cran.r-project.org/web/packages/pheatmap</a>

**RESOURCE AVAILABILITY**

**Lead contact**

Further information and requests for resources and reagents should be directed to and will be fulfilled by the lead contact, Ning Zhang ([zhangning@bjmu.edu.cn](mailto:zhangning@bjmu.edu.cn)).

**Materials availability**

Distribution of organoids to third (academic or commercial) parties upon reasonable request requires approval by an internal review board and completion of a material transfer agreement in order to ensure compliance with medical research involving human subjects' act. Use of organoids is subjected to patient consent; upon consent withdrawal, distributed organoid lines and any derived material will have to be promptly disposed.

**Data and code availability**

DNA and RNA sequencing data have been deposited at [Genome Sequence Archive for Human](https://www.ncbi.nlm.nih.gov/genome/sequence_archive/) HRA006499 and are publicly available as of the date of this publication. Accession numbers are listed in the [key resources table](#). All data from the TCGA database are available at <https://xena.ucsc.edu/>. All molecular data for CCLE cancer cell lines are available at <https://depmap.org/portal/>. All software is freely or commercially available and is listed in the STAR Methods description and key resources table. Any additional information required to reanalyze the data reported in this paper is available from the lead contact upon request.

**EXPERIMENTAL MODELS AND STUDY PARTICIPANT DETAILS**

**Sample collection and patient information**

Primary liver cancer (PLC) specimens were obtained from patients who underwent surgical excision of PLC at Henan Cancer Hospital (Henan province, China), the 302th Hospital of Chinese PLA (Beijing, China) and Peking University Cancer Hospital (Beijing, China). All patient samples in this study were collected with informed consent in accordance with the Declaration of Helsinki. The study was approved by hospital ethics committees (2016CT054 and 2019-002-D). [Table S1](#) summarizes clinical data of each patient.

Tissue samples were stored in F12/DMEM medium with 1% v/v penicillin/streptomycin solution (Gibco) and transported to the laboratory on ice. Each region of tissue sample was split into at least two sections, used for histological analysis and organoid culturing respectively. For big samples, one more section was cut for DNA and RNA isolation to be used for WES and RNA-seq profiling. A total of 528 regions from 144 PLC patients were sampled and organoid cultures were successfully established for 399 regions. For 14 patients with relapse during the study period, patient response to therapeutic treatment was evaluated based on mRECIST criteria.<sup>62</sup>

### Tissue dissociation and organoid culturing

Tissue was minced into small pieces (approximate 0.5–1 mm diameter) using fine dissection scissors, and then rinsed 3 times with phosphate buffered saline (PBS; Thermo Fisher Scientific) at 4°C in 50-mL Falcon tubes. The minced pieces of tissue were then dissociated using tumor dissociation kit (Milenyi Biotec) following the manufacturer's instructions. Incubation (37°C) ranged from 30 to 90 min (depending on the amount of tissue) until the majority of cells were in suspension. Digestion was stopped by adding cold DMEM supplemented with 10% FBS. Cells were filtered through a 70 μm Nylon cell strainer, followed by spinning (5 min at 500 g). Cells were incubated in 1X RBC lysis buffer (Thermo Fisher Scientific) under gentle rotation for 10 min at 4°C to lyse contaminating red blood cells. After RBC lysis buffer was aspirated, cells were mixed with 30% growth factor–reduced Matrigel (Corning) and seeded into ultralow-attachment 24- or 48- well plates according to the number of live cells. After Matrigel was solidified within 30 min, warm organoid isolation culture medium was added.

The isolation medium was based on a previous report<sup>23</sup> with minor modifications including replacing Noggin, Rspo-1 and Wnt3a-conditioned media with 25 ng/mL recombinant human Noggin (PeproTech), 500 ng/mL Rspo-1 (Novoprotein) and 100 ng/mL Wnt3a (SAB). The expansion medium (for passage 2 and later passage) was comprised of Advanced DMEM/F12 supplemented with 1% penicillin/streptomycin, 1% glutamax, 10-mM HEPES, 1:50 B27 supplement (without vitamin A), 1:100 N2 supplement, 1.25 mM N-acetyl-L-cysteine (Sigma), 10-mM nicotinamide, 10-nM recombinant human (Leu15)-gastrin I, 50 ng/mL recombinant human EGF, 100 ng/mL recombinant human FGF10, 25 ng/mL recombinant human HGF, 10 μM forskolin, 5-μM A83-01, 10 μM Y27632 (Sigma), 25 ng/mL recombinant human Noggin, 500 ng/mL Rspo-1 and 100 ng/mL Wnt3a. The culture medium was replenished with fresh media every 3–4 days. Organoid cultures were passaged at a 1:2–4 dilution every 1–3 weeks by mechanical dissociation or using 0.25% Trypsin-EDTA into small fragments. For preparing frozen stocks, organoid cultures were dissociated into singles cell or small pieces and then frozen in 90% CS-FBS and 10% DMSO in –80°C. Cryopreserved stocks have been successfully recovered for up to approximately 18 months after freezing.

Regarding the clinical/histological characteristics of liver cancer patients associated with organoid establishment rate, tumors from clinical stage II/III/IV patients have significantly higher successful rate ( $p < 0.05$ ) (Data S1.6), as indicated previously.<sup>23,28</sup>

Further, to investigate the experimental factors influencing establishment rate, we collected 30 samples from PLC patients and randomly divided each sample for six aliquots, for organoid modeling using different experimental procedures (Data S1.7). As a result, the proportion of living cells, sample acquisition time and methods of digestion showed a great impact in the successful rate. However, our establishment rate (75.6%) could be compromised in a real clinical scenario with more complicated logistic issues affecting the proportion of viable cells, as indicated by a recent multi-centre study.<sup>28</sup>

All developed tumor organoids ( $n = 399$ ) have been the evaluated of cell morphology, by two independent pathologists based on H&E staining. In addition, 159 ones were further tested for tumor properties using at least one of three methods (identification of driver gene mutations, xenografting, aneuploidy analysis).

### Organoid-derived tumor xenograft

Four-week-old male BALB/c mice were ordered from Center of Experimental Animals (Peking University First Hospital, Beijing, China), and bred under pathogen-free conditions. All mouse experiments were approved by the Institutional Animal Care and Use Committee of Peking University First Hospital.

For subcutaneous grafts, 5 million organoid-dissociated cell suspensions were prepared in 10% Matrigel/90% F12/DMEM. Two weeks after inoculation, when the tumor volumes reached approximately 200 mm<sup>3</sup>, mice were randomly divided into different groups ( $n = 5$  each). To test the effect of drug treatment in inhibiting tumor *in situ*, mice were treated with Lenvatinib (10 mg kg<sup>-1</sup>, oral gavage), Veratramine (10 mg kg<sup>-1</sup>, oral gavage), PKUF-01 (10 mg kg<sup>-1</sup>, oral gavage), or Lenvatinib combined with Veratramine (10 mg kg<sup>-1</sup> each, oral gavage) every day in the following 3 weeks. Tumor volume was measured every day and quantified every five days using the formula: tumor volume =  $\frac{1}{2}$  length  $\times$  width.<sup>2</sup> The significance of tumor volume was assessed by ANOVA and post hoc Tukey HSD test. All mice were sacrificed after a total of five weeks.

## METHOD DETAILS

### Histology and immunostaining

Tissues and organoids were fixed for 24 h and 0.5 h respectively, in 10% neutral buffered formalin (Sigma-Aldrich) at room temperature, and then embedded in paraffin. It was cut at 5 μm and stained according to the standard Hematoxylin and Eosin (H&E) and immunohistochemistry (IHC) staining protocols. For IHC, primary antibodies against CK7, KRT19, HepPar1, AFP, c-Jun, JNK, β-catenin (Abcam) were used at the dilution of 1:200. Immunostaining was scored considering both staining intensity and extent. Staining intensity was classified as 0 (negative), 1 (weak), 2 (moderate) and 3 (strong). Staining extent dependent on the percentage of positive

tumor cells were divided into 0 (<5%), 1 (5–25%), 2 (26–50%), 3 (51–75%), and 4 (>75%). The final score was determined by multiplying the intensity and the quantity scores, which yielded a range from 0 to 12.

### WES sequencing and data pre-processing

For each tumor organoid/tissue sample, normal tissue or blood sample from the same patient was used as normal control. Genomic DNA was isolated using DNeasy & RNeasy isolation kit (Qiagen) and exon regions were captured by Agilent SureSelectXT Human All Exon V6 probes. DNA libraries were sequenced by Illumina NovaSeq 6000 platform and 150 bp paired-end reads were generated. WES achieved a median of  $\times 233$  depth for tumor tissues,  $\times 236$  for PDOs, and  $\times 249$  for normal controls. Quality control of raw reads was performed by FastQC (v0.11.9), Cutadapt (v2.5 with Illumina universal adapters) and Trimmomatic (v0.39 with PE, MINLEN\_36) tools. Clean reads were aligned to UCSC human reference genome (hg19) using bwa-mem2 (v2.0)<sup>49</sup> with default parameters. Merging, coordinate sorting and indexing of binary aligned sequencing (BAM) files were performed using Samtools (v1.10). PCR and optical duplicates were removed by Genome Analysis Toolkit (GATK) (v4.1.2.0). Sequencing coverage metrics were generated by Samtools, based on the exonic regions specified by the target BED file (SureSelectAllExonV6r2). Median WES coverage was  $\times 233$  for tumor tissue (n = 99)  $\times 236$  for PDO (n = 99), and  $\times 249$  for normal control (n = 36). More details were listed in [Table S2](#), [S3](#) and [S4](#).

### Somatic mutation calling

Somatic point mutations and small indels were called using the Mutect2 (version 4.1.2.0) pipeline for paired tumor-normal samples with normal tissue or blood from the same patient used as control. Briefly, Mutect2 was applied to call somatic variants for each pair of tumor-normal BAM file, and the generated VCF files were refined using the following filtering criteria: 1) at least  $\times 10$  coverage of wild type allele in normal sample with at most one read harboring mutant allele; (2) at least  $\times 10$  total coverage in tumor samples with at least 3 reads supporting mutation allele; (3) reads with mean base quality  $< 20$  at each variant position were excluded. The identified candidate variants were further filtered by population frequency ( $< 1\%$  kept) in the ExAC database, gnomAD\_exome (v2.1.1) and 1000Genome (August 2015). Somatic variants were annotated using ANNOVAR. Liver cancer-related genes were curated from published liver cancer genomic studies, including genes from our previous study<sup>15</sup> and genes from a previous study of PLC organoids.<sup>23</sup> Regarding the comparison of concordant non-silent mutations in cancer-related genes between tissue-organoid pairs and between multi-region samples, we manually checked all inconsistent variants to rescue the potentially missed ones due to tumor purity, according to a published strategy.<sup>23</sup> All identified non-silent somatic mutations were summarized in [Table S2](#) (organoids) and [Table S3](#) (tumor tissues). Tumor mutation burden was computed as the sum of all non-silent mutations per tumor divided by the total number of captured bases by Agilent v6 (38.3 Mb).

### Copy number calling

Copy number alterations (CNAs) was estimated using CNVkit with the default parameters. Significantly recurrent CNAs were identified using GISTIC2.0<sup>53</sup> with the default threshold ( $q < 0.25$ ). And the significant CNAs were used for comparing copy number profile of organoids and tissues. Liver cancer genes within frequent CNA segments were adopted from our previous study.<sup>15</sup>

### Phylogenetic tree

For multi-regional organoids sampled from a same tumor, we inferred a phylogenetic tree based on their genomic profiles as described in our previous study.<sup>15</sup> Briefly, genomic sequences ( $\pm 20$  bp from the mutation position) of each sample were extracted to construct the phylogenetic trees by using MEGA5 with maximum-parsimony algorithm. Potential driver genomic events were labeled on each tree's root, stem, clade and leaf, based on the clonal relationship. We adopted our previously reported metrics Mut-ITH and CNA-ITH,<sup>13</sup> to quantify genomic ITH levels of each patient, which were listed in [Table S5](#).

### RNA-seq and quantification

Total RNA was isolated using DNeasy & RNeasy isolation kit (Qiagen) and purified using poly-T oligo-attached magnetic beads. RNA libraries were also sequenced by Illumina NovaSeq 6000 platform and 150 bp paired-end reads were generated. Quality control of raw reads was performed by FastQC (v0.11.9), Cutadapt (v2.5 with Illumina universal adapters) and Trimmomatic (v0.39 with PE, MINLEN\_36) tools. STAR software (v2.7.3a) was used to align reads to the reference human genome hg19 with default parameters. Gene-level read counts were generated by applying HTseq-count with the GENCODE annotations, and transcript per million (TPM) values were calculated using RSEM.<sup>58</sup> Unless specified,  $\log_2$  (TPM+1) was referred as mRNA expression level in this study. The correlation heatmap between tissue-organoid pairs was plotted as previously described.<sup>21</sup> Average expression of target genes of Sorafenib and Lenvatinib (Sorafenib targets: *VEGFR2*, *VEGFR3*, *BRAF*, *RAF*, *PDGFRB*, *KIT*, *FIT3*; Lenvatinib targets: *VEGFR1*, *VEGFR2*, *VEGFR3*, *FGFR1*, *FGFR2*, *FGFR3*, *FGFR4*, *PDGFRA*, *PDGFRB*, *KIT*, *RET*) were used for [Figures 2F](#) and [S2D](#), with  $\log_{10}$  transformed expression of all 3,804 potential housekeeping genes that are expressed uniformly across different tissues<sup>63</sup> used as the reference control. Significance of the expression variance between multi-samples was determined by ANOVA.

### Drug screening

In total, seven anti-tumor agents used in clinical practices, three c-Jun inhibitors and a compound (PKUF-01) were used for drug screening. All drugs were dissolved in DMSO and stored at  $-80^\circ\text{C}$ . Organoids were digested into small spheres within 70  $\mu\text{m}$ . For organoids could not be digested well by mechanical dissociation or 0.25% Trypsin-EDTA, we passed through a 70  $\mu\text{m}$  cell strainer

to eliminate large organoids. Organoids were seeded into ultralow-attachment 96-well plates or 384-well plates at the density of approximately 100 organoids per 100 $\mu$ l in 5% Matrigel/culture medium. As suggested by a previous study,<sup>64</sup> Y-27632 and A8301 were removed from the complete culture medium, due to the consideration that these inhibitors might have some potential effects on specific signaling pathways affecting the results of drug screening. After plating, a 7-point 5–10 -fold dilution series of each drug was dispensed. Drug concentrations ranged from 50 $\mu$ M, 10 $\mu$ M, 1 $\mu$ M, 0.1 $\mu$ M, 0.01 $\mu$ M, 0.001 $\mu$ M and 0 $\mu$ M (denoted as control), and maximal DMSO concentration used was 1%. Cell viability was analyzed using CCK8 assay according to the manufacturer's instructions following 6 days of drug incubation, and results were normalized to corresponding control. Data analyses were performed using GraphPad Prism 9 software, the values of IC<sub>50</sub> and AUC were calculated by applying nonlinear regression (curve fit) and the equation  $\log(\text{inhibitor})$  versus normalized response.<sup>65</sup> Each dilution of drugs was performed at least in triplicate. The AUC or IC<sub>50</sub> values of organoids treated with each drug were listed in Table S6.

The maximum IC<sub>50</sub> (or AUC) value among all regions from a patient were defined as the patient-level IC<sub>50</sub> (or AUC) value, based on the assumption that a patient's response to a drug treatment was determined by the most resistant region. All patients were ranked by patient-level AUC and dichotomized into sensitive and resistant groups for each drug respectively, using the percentile cutoff according to the reported clinical overall response rate (ORR), which were 24.1% for Lenvatinib,<sup>6</sup> 9.2% for Sorafenib,<sup>6</sup> 11% for Regorafenib,<sup>7</sup> 10.7% for Apatinib,<sup>66</sup> and 3% for Bevacizumab.<sup>67</sup> Although some ORRs were from clinical trials of HCC patients due to a current lack of studies with both HCC and ICC included, they were reasonable approximations of all PLC patients as HCC accounts for 90% PLC patients<sup>5</sup> and 86.6% organoids in the biobank. Additionally, due to the lack of WES/RNA-seq profiles for all organoids, we made an assumption of 1% for the proportion of sensitive organoids to treatment of Pemigatinib and Ivosidenib in the biobank, as Pemigatinib<sup>32</sup> and Ivosidenib<sup>33</sup> targeting ICC patients harboring low-frequency mutations (10–16% for FGFR2 rearrangements and approximately 13% for IDH1 mutations)<sup>32,33</sup> and ICC patients accounted for 15.5% of total organoids we generated.

### Differential gene expression and gene set enrichment analysis

Differential expressed genes (DEGs) between the drug sensitive and resistant groups were identified by DESeq2 with absolute fold change >2 and adjusted p value <0.05. The ranks of DEGs were used for GSEA analysis with a published stem cell gene set<sup>23</sup> and GO\_BP gene sets (MSigDB V7.5.1). Significant enrichment was considered as  $q < 0.25$ . KEGG and GO pathway enrichment analyses of genes of interest were performed using ClusterProfiler. A previously-reported HCC transcriptome subtype<sup>29</sup> was tested in our HCC transcriptome profiles by applying nearest template prediction (NTP) algorithm (GenePattern module), and the consistency of predicted subtypes between tissue-organoid pairs was assessed by Fisher's exact test.

### Machine learning model of drug response

To model the drug response with transcriptome data, we applied a bootstrap strategy using LASSO (least absolute shrinkage and selection operator) regression models to develop expression signatures for predicting treatment response of five drugs (Lenvatinib, Sorafenib, Regorafenib, Apatinib, and PKUF-01) following a similar strategy employed in ReProMSig.<sup>68</sup> In brief, candidate genes were first selected based on expression associations with individual drug response in the training set ( $n = 106$ ), with a stepwise increase (0.01 per increase) of correlation coefficients and a limit on the number of identified candidate genes (100–1,000). Multiple sets of candidate genes were then selected and used for building each specific prediction model respectively. A LASSO regression model was applied to model drug sensitivity profile ( $-\log_2$  of IC<sub>50</sub> value) with expression profiles of a set of selected candidate genes, which was implemented using the *glmnet* package (v4.1-3) with the optimum penalty parameter 'lambda' chosen by 10-fold cross-validation. The regression modeling process was bootstrapped ( $n = 100$ ), and candidate genes regarded as important genes in more than 50% occurrences, were taken as signature genes for final modeling. The optimal model with a specific correlation coefficient cutoff was then obtained by fitting the chosen signature genes. AUROCs of all models associated with an individual drug were compared to find the optimal threshold of correlation coefficient, which was 0.28 for Lenvatinib, 0.63 for Sorafenib, 0.29 for Regorafenib, 0.34 for Apatinib, and 0.27 for PKUF01, respectively. ROC curve and AUROC were analyzed by the ROCR package (v1.0-11).

The validation set consists of another 106 organoids, which were established prospectively using samples from Henan Provincial Tumor Hospital (Henan, China). The final model for each drug was evaluated on the validation set respectively, by ROC curves. The 11 patients with transcriptome and drug response were involved in the validation of signature prediction and clinical response.

### Plasmids and transfection

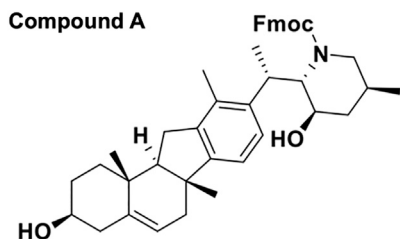
Plasmids used in the study, including 3 $\times$ Flag, Flag-c-Jun, Flag-JNK, Flag- $\beta$ -catenin, sh NC, sh c-Jun, sh JNK, sh  $\beta$ -catenin, mutant  $\beta$ -catenin and constitutive active JNK, were ordered from Mailgene biosciences co., ltd. (Beijing, China). By using Lipofectamine 3000 (Invitrogen), we transfected digestive organoids cells with indicated plasmid following the previously reported protocol.<sup>69</sup> When the neomycin phosphotransferase gene (*neo*) in cells were expressed, organoids showed potent resistance to G418. Transfected organoids were selected by organoid culture medium adding additional 400  $\mu$ g/ml G418 (GIBCO) for 14 days.

### Synthesis of PKUF-01

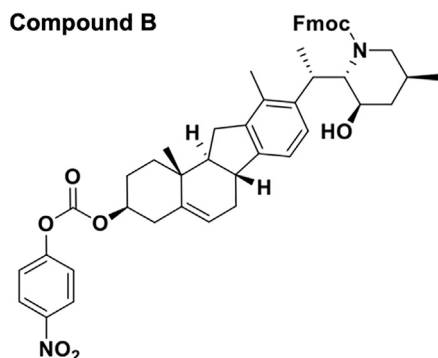
The PKUF-01 compound used in this study was synthesized by our laboratory, consisting of five steps as illustrate below.

Step 1: Adding Veratramine (200 mg, 0.5 mmol) and fluorene methoxycarbonyl chloride (145 mg, 0.6 mmol) in order in an eggplant-shaped reaction bottle, and 20 mL dichloromethane was introduced to dissolve this mixture. Followingly, triethylamine

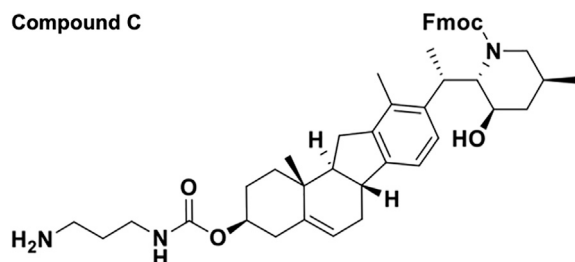
(60 mg, 0.6 mmol) was added and stirred at room temperature for 1 h until the reaction was complete. After vacuum concentration, the crude product was separated and purified by column chromatography to obtain compound A, a white solid, with a yield of 88%.



Step 2: Adding compound A (133 mg, 0.2 mmol) and *p*-nitrophenyl chloroformate (51 mg, 0.25 mmol) in order in an eggplant-shaped reaction bottle, and 20 mL of dichloromethane was used to dissolve this mixture. Followingly, pyridine (24 mg, 0.3 mmol) was added and stirred at room temperature for 1 h until the reaction was complete. After vacuum concentration, the crude product was separated and purified by column chromatography to obtain compound B, a white solid, with a yield of 90%.



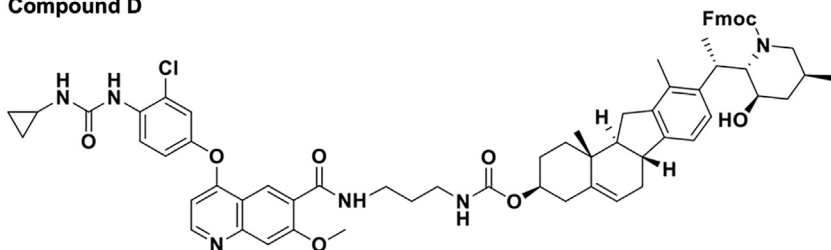
Step 3: Adding compound B (150 mg, 0.2 mmol) and 1,3-propanediamine (15 mg, 0.2 mmol) in order in an eggplant-shaped reaction bottle, and 20 mL dichloromethane was used to dissolve this mixture. Followingly, *N,N*-diisopropylethylamine (DIPEA, 49 mg, 0.4 mmol) was added and stirred at room temperature for 1 h until the reaction was complete, after vacuum concentration, the crude product was separated and purified by column chromatography to obtain compound C, a white solid, with a yield of 87%.



Step 4: Adding 4 - (3-chloro-4 - (3-cyclopropylurea) phenoxy) - 7-methoxyquinoline-6-carboxylic acid (64 mg, 0.15 mmol) and 2 - (7-azabenzotriazole) - *N,N,N',N'* - tetramethylurea hexafluorophosphate (HATU, 76 mg, 0.2 mmol) successively in an eggplant-shaped reaction bottle, and 20 mL dichloromethane was used to dissolve them. Followingly, DIPEA (49 mg,

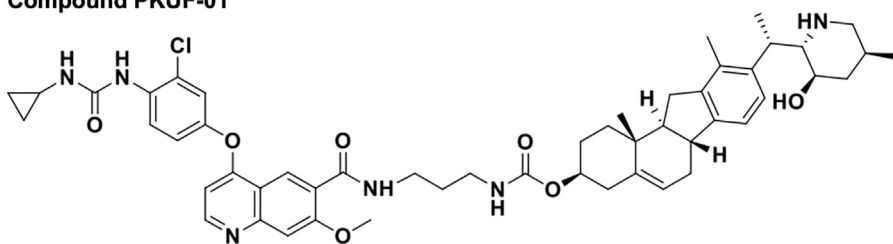
0.4 mmol) was added and stirred at room temperature for 15 min, and then compound C (112 mg, 0.15 mmol) was added and stirred at room temperature for another hour until the reaction was complete. After vacuum concentration, the crude product was separated and purified by column chromatography to obtain compound D, a white solid, with a yield of 83%.

**Compound D**



Step 5: Adding compound D (116 mg, 0.12 mmol) into an eggplant-shaped reaction bottle, and 20 mL 20% methylpiperidine DMF solution was used to dissolve this mixture, followed by stirring at room temperature for 15 min until the reaction was complete. After vacuum concentration, the crude product was separated and purified by column chromatography to obtain compound PKUF-01, a white solid, with a yield of 95%.

**Compound PKUF-01**



**QUANTIFICATION AND STATISTICAL ANALYSES**

Where applicable, statistical methods are outlined in the respective figure legends. Statistical analysis was performed utilizing GraphPad and R software. *p* values were calculated using a two-tailed Wilcoxon test. Spearman correlation was used for gene-drug analysis. DNA and RNA sequencing analysis details can be found in the relevant [STAR methods](#) sections.